Magnetic field tuning of low-energy spin dynamics in the single-atomic magnet Li2(Li1−xFex)N

S. A. Bräuninger, Anton Jesche, S. Kamusella, F. Seewald, M. Fix, R. Sarkar, A. A. Zvyagin, H.-H. Klauss

Angaben zur Veröffentlichung / Publication details:

Bräuninger, S. A., Anton Jesche, S. Kamusella, F. Seewald, M. Fix, R. Sarkar, A. A. Zvyagin, and H.-H. Klauss. 2020. "Magnetic field tuning of low-energy spin dynamics in the single-atomic magnet Li2(Li1−xFex)N." *Physical Review B* 102 (5): 054426. https://doi.org/10.1103/physrevb.102.054426.

Magnetic field tuning of low-energy spin dynamics in the single-atomic magnet $Li_2(Li_{1-x}Fe_x)N$

S. A. Bräuninger,[1] A. Jesche,[2] S. Kamusella,[1] F. Seewald,[1] M. Fix,[2] R. Sarkar,[1] A. A. Zvyagin,[3,4,5] and H.-H. Klauss[1]

[1]*Institute of Solid State and Materials Physics, TU Dresden, D-01069 Dresden, Germany*

[2]*Institute of Physics, University Augsburg, D-86135 Augsburg, Germany*

[3]*Max-Planck-Institute for the Physics of Complex Systems, Nöthnitzer Str. 38, D-01187 Dresden, Germany*

[4]*B.I. Verkin Institute for Low Temperature Physics and Engineering of the National Academy of Sciences of Ukraine, Nauky Ave. 47, 61103 Kharkiv, Ukraine*

[5]*V.N. Karazin Kharkiv National University, Svobody sq. 4, 61022 Kharkiv, Ukraine*

(Received 30 September 2019; revised 1 May 2020; accepted 21 July 2020; published 19 August 2020)

We present a systematic ^{57}Fe Mössbauer study on highly diluted Fe centers in $Li_2(Li_{1-x}Fe_x)N$ single crystals as a function of temperature and magnetic field applied transverse and longitudinal with respect to the single-ion anisotropy axis. Below 30 K, the Fe centers exhibit a giant magnetic hyperfine field of $\bar{B}_A = 70.25(2)$ T parallel to the axis of strongest electric field gradient $\bar{V}_{zz} = -154.0(1)$ V/Å^2. Fluctuations of the magnetic hyperfine field are observed between 50 and 300 K and described by the Blume two-level relaxation model. From the temperature dependence of the fluctuation rate, an Orbach spin-lattice relaxation process is deduced. An Arrhenius analysis yields a single thermal activation barrier of $\bar{E}_A = 570(6)$ K and an attempt frequency $\bar{\nu}_0 = 309(10)$ GHz. Mössbauer spectroscopy studies with applied transverse magnetic fields up to 5 T reveal a large increase of the fluctuation rate by more than one order of magnitude. In longitudinal magnetic fields, a splitting of the fluctuation rate into two branches is observed consistent with a Zeeman induced modification of the energy levels. The experimental observations are qualitatively reproduced by a single-ion effective spin Hamiltonian analysis assuming a Fe^{1+} d^7 charge state with the unquenched orbital moment and a $J = 7/2$ ground state. It is demonstrated that a weak axial single-ion anisotropy D of the order of a few Kelvin can cause a two orders of magnitude larger energy barrier for longitudinal spin fluctuations.

DOI: 10.1103/PhysRevB.102.054426

I. INTRODUCTION

Single-molecule magnets (SMMs) and single-atomic magnets (SAMs) are model systems to study fundamental aspects of magnetic relaxation including quantum tunneling of magnetization and quantum coherence in nanoscale systems [1,2]. Moreover, SMMs and SAMs are proposed for novel data storage devices in spintronics or possible applications for quantum computing [3–5].

Isolated magnetic moments with strong axial anisotropy exhibit a bistability of magnetization with an energy barrier to magnetization reversal resulting in slow magnetic relaxation. Fluctuation of magnetization is driven by spin-lattice relaxation or hyperfine coupling processes. For thermally activated fluctuations, the spin relaxation time τ at a temperature T is described by

$$\tau = \tau_0 \exp\left(\frac{E_A}{k_B T}\right), \tag{1}$$

controlled by an effective energy barrier E_A, an "attempt time" τ_0, and with the Boltzmann constant k_B. The experimentally observed energy barrier E_A can be very different from the magnetic anisotropy energy $E_m = DS^2$. Magnetic quantum tunneling processes via degenerate S_z states above the $\pm S$ ground state can considerably reduce E_A. External magnetic fields applied longitudinal to the magnetic anisotropy axis can be used to tune the magnetic system through the level crossing condition for specific S_z states via Zeeman interaction. However, quantum tunneling can only occur if off-diagonal elements in the spin Hamiltonian cause a mixing of these S_z eigenstates and an avoided level crossing with a finite minimum energy gap $\Delta_{m,m'}$ is generated. The Landau-Zener model [6] is applied to describe the magnetic quantum tunneling observed via magnetization steps in low-temperature magnetization experiments, e.g., in nanomagnets such as Mn_{12}-ac [7] or $[Fe_8\,O_2(OH)_{12}(tacn)_6]^{8+}$, briefly Fe_8 [8]. In an external magnetic field applied transverse to the anisotropy axis, the quantum tunneling can be modulated by quantum interference [9]. This topological quantum phase interference, described by a Berry phase, is experimentally observed [10].

$Li_2(Li_{1-x}Fe_x)N$ crystallizes in a hexagonal symmetry (space group $P6/mmm$) and alternating planes of (Li_2N) and $(Li_{1-x}Fe_x)$ are stacked along the crystallographic c axis [11]. Figure 1 shows the enhanced unit cell emphasizing the hexagonal symmetry of the Fe site and the corresponding linear N-Fe-N geometry. In Li_3N, each N^{3-} ion is surrounded by eight Li^+ ions. Six Li^+ are located in plane in a hexagonal geometry (Li-2c sites). Two Li^+ (Li-1b sites) are located between the planes leading to a hexagonal-bipyramidal geometry. The Fe ions occupy only the Li-1b site in between the Li_2N planes. Studies on polycrystalline samples of concentrated $Li_2(Li_{1-x}Fe_x)N$ with $x \approx 0.16$ and ≈ 0.21

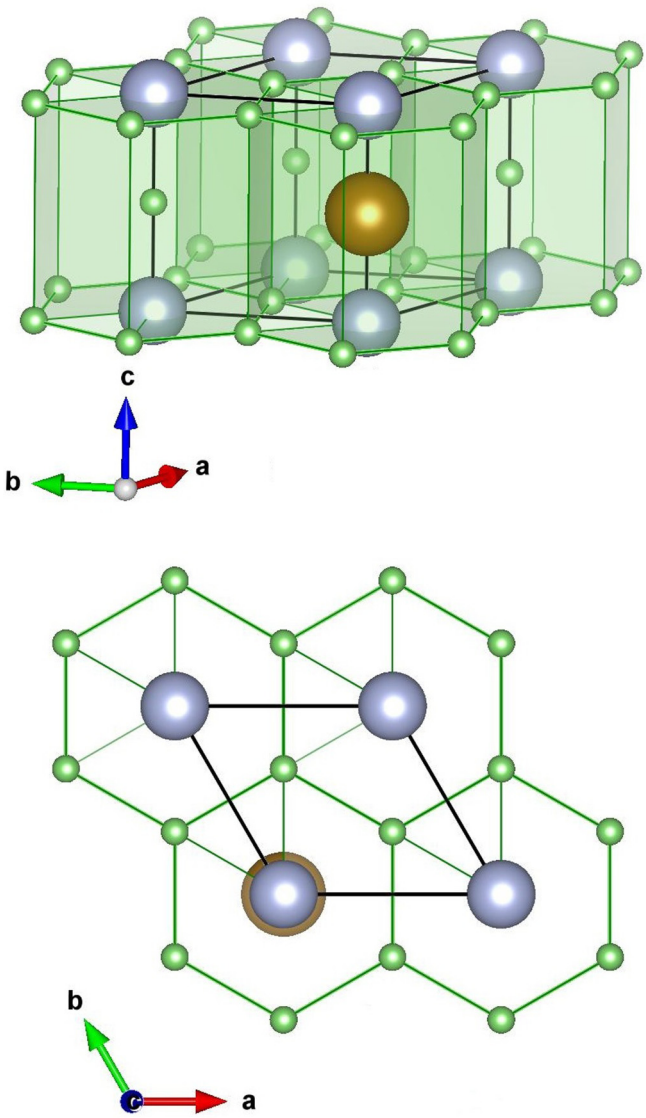

FIG. 1. Crystal structure of $Li_2(Li_{1-x}Fe_x)N$ [11]. The host system is an α-Li_3N matrix, here Li^+ shown in green (2*c* Wyckoff site, in-plane) and N^{3-} in gray (1*a* Wyckoff site). Fe substitution, shown in brown, takes place only between the N^{3-} (1*b* Wyckoff site). The black lines show the primitive unit cell.

by Mössbauer spectroscopy revealed a static hyperfine field below $T_C \approx 65$ K and long-range ferromagnetic ordering was proposed on the basis of magnetization studies [12,13]. More recently, magnetization studies on large single crystals of $Li_2(Li_{1-x}Fe_x)N$ with $x = 0.001$–0.3 were reported [14,15]. Large magnetic moments exceeding the spin-only value with a strong axial anisotropy parallel to the *c* axis are found. These magnetic moments can be associated with isolated Fe ions linearly coordinated with two nitrogen ions in covalent N-Fe-N bonds [16]. From low-temperature magnetization experiments on single crystals a magnetic anisotropy field of $B \approx 88$ T ($x \approx 0.0032$) was estimated together with a large effective magnetic moment $\mu_{\text{eff}} = 6.5(4)\mu_B$ per Fe atom parallel to the *c* axis, largely independent of the Fe concentration [14]. For $x \approx 0.28$, an even larger magnetic anisotropy field of $B \approx 220$ T was reported [14]. The deduced value of μ_{eff} is in agreement with the fully spin-orbit coupled Hunds rule value of an Fe^{1+} configuration [12,14]. The observation of steps in magnetic hysteresis loops and relaxation phenomena with an energy barrier $E_B \approx 430$ K indicate a SMM-like behavior. The relaxation time is only weakly temperature-depended below 10 K indicating the importance of quantum tunneling in this temperature range [16]. However, the microscopic process of the thermally excited relaxation is not known. At low Fe doping concentrations, data suggest that the spontaneous magnetization and hysteresis is not caused by a collective magnetic ordering but rather due to the strong axial magnetic anisotropy in the linear N-Fe-N moiety [14]. A recent study reports a slow paramagnetic relaxation stressing the proposed ferromagnetic nature of nondiluted $Li_2(Li_{1-x}Fe_x)N$ ($x \approx 0.30$) [15].

Xu *et al.* [17] performed electronic structure calculations for $Li_2(Li_{1-x}Fe_x)N$, which reveal large magnetic anisotropy energies of 305 K for an Fe^{2+} d^6 with $J = 4$ configuration and 360 K for Fe^{1+} d^7 with $J = 7/2$ configuration. Moreover, the authors propose that an Fe^{2+} state could dominate at low $x \ll 1$, whereas the Fe^{1+} state should play the major role at larger x. However, it is not clear how such strong axial anisotropy energies around 300 K can be reconciled with the observation of electronic level crossings in the magnetic hysteresis experiments at very low longitudinal magnetic fields of $B_L = 0.15$, 0.55, and 3 T [14,16], i.e., energy scales $\mu B/k_B$ of several degrees Kelvin only.

To address these questions, in this manuscript we report a detailed ^{57}Fe Mössbauer investigation on single crystals of highly diluted Fe in $Li_2(Li_{1-x}Fe_x)N$ with $x = 0.0275$, 0.0109, 0.0099, and 0.0013. The measurements were performed at temperatures 2 K $\leqslant T \leqslant$ 300 K in magnetic fields 0 T $\leqslant B \leqslant$ 5 T applied transverse and longitudinal to the crystallographic *c* axis (magnetically easy axis). Below $T =$ 30 K, the Fe centers exhibit a giant magnetic hyperfine field of $\bar{B}_A = 70.25(2)$ T parallel to the axis of strongest electric field gradient $\bar{V}_{zz} = -154.0(1)$ V/Å^2. We demonstrate that the diluted Fe ions in $Li_2(Li_{1-x}Fe_x)N$ indeed form isolated single-ion paramagnets consistent with an Fe^{1+} d^7 charge state and an unquenched orbital moment, i.e., total angular momentum $J = 7/2$. A continuous slowing down of the spin fluctuations is observed by Mössbauer spectroscopy below $T = 300$ K, which can be described by a thermally activated Orbach process with an activation barrier of $\bar{E}_A = 570(6)$ K. The fluctuation rate is very sensitive to magnetic fields of the order of a few Tesla even at elevated temperatures of $T \sim 70$ K. A quasistatic magnetic hyperfine field is observed below 50 K. A clustering of nearest neighbor Fe ions is ruled out by studies on samples with four different $x \leqslant 0.028$ proving the single-atomic-magnet behavior. The experimental observations are qualitatively reproduced by a single-ion spin Hamiltonian analysis. It is demonstrated that, for dominant magnetic quantum tunneling relaxation processes, a weak axial single-ion anisotropy D of the order of a few Kelvin can cause a two orders of magnitude larger energy barrier E_B for longitudinal spin fluctuations in systems with a large angular momentum quantum number. The slow spin fluctuations at low temperatures suggest $Li_2(Li_{1-x}Fe_x)N$ to be a candidate for a novel functional magnetic materials, e.g., in quantum computing.

TABLE I. Fe concentration x and estimated error Δx in $Li_2(Li_{1-x}Fe_x)N$ determined by ICP-OES.

	x (%)	Δx (%)	also denoted as
SC 1	2.75	0.16	$Li_2(Li_{0.9725}\ Fe_{0.0275})N$
SC 2	1.09	0.07	$Li_2(Li_{0.9891}\ Fe_{0.0109})N$
SC 3	0.99	0.06	$Li_2(Li_{0.9901}\ Fe_{0.0099})N$
SC 4	0.13	0.01	$Li_2(Li_{0.9987}\ Fe_{0.0013})N$

II. EXPERIMENTAL

Four single crystals (SCs) were investigated by ^{57}Fe Mössbauer spectroscopy in this work. The crystals were grown out of lithium rich flux [18]. The starting materials Li_3N powder (Alfa Aesar, 99.4%), Li granules (Alfa Aesar, 99%), and Fe granules (Alfa Aesar 99.98%) were mixed in a molar ratio of Li:Fe:$Li_3N = 6 - x : x : 1$ with $x = 1.5,\ 0.5,\ 0.5$, and 0.1 for samples SC 1, SC 2, SC 3, and SC 4, respectively. The mixtures with a total mass of roughly 1.5 g were packed into a three-cap Nb crucible [19] inside an argon-filled glovebox. The crucibles were sealed in ∼0.6 bar Ar via arc welding and finally sealed in a silica ampule in ∼0.2 bar Ar. The mixtures were heated to $T = 900\ ^\circ$C within 5 h, cooled to $T = 750\ ^\circ$C over 1.5 h, slowly cooled to $T = 500\ ^\circ$C over 60 h and finally decanted to separate the crystals from the excess flux. The composition was determined by inductively coupled plasma optical emission spectroscopy (ICP-OES) using a Vista-MPX. To this end the samples were dissolved in a mixture of hydrochloric acid and distilled water. Obtained Fe concentrations based on the measured Li:Fe ratio are given in Table I.

Mössbauer measurements were carried out in CryoVac and Oxford instruments helium flow cryostats in under-pressure mode or normal mode, respectively. We used a WissEl Mössbauer spectrometer. The detector was a proportional counter tube or a Si-PIN-detector from KETEK. A Rh/Co source with an initial activity of 1.4 GB was used. The superconducting coil was powered by an Oxford instruments IPS 120-10 power supply with an applied magnetic field parallel or perpendicular to the γ beam with an angle error of $<5^\circ$. The absorber SC 1 exceeded the thin absorber limit requiring a transmission integral fit. The analysis was done using the MOESSFIT analysis software [20]. All measurements were performed with the γ beam parallel to the crystallographic c axis. The single crystals were protected by paraffin wax to avoid oxidation.

III. RESULTS

A. Macroscopic magnetization

Magnetization measurements were performed using a 7 T Magnetic Property Measurement System (MPMS), manufactured by Quantum Design. Figure 2 shows the isothermal magnetization of SC 1 measured at different temperatures for magnetic field applied parallel to the crystallographic c axis, $B_L \parallel c$, i.e., parallel to the Fe ion anisotropy axis. The effective sweep rate for the full loops was 2.9 mT/s with 10 mT/s between the measurements. Hysteresis emerges for temperatures $T < 50$ K. At $T = 2$ K, steps appear at $\mu_0 B_L \approx 0$ and ±3.3 T as well as for $\mu_0 B_L = 0.55$ T, with the latter being recognizable only in the derivative dM/dB. At lower x, additional steps appear at $\mu_0 B_L = 0.15$ T and the anomalies become sharper [14,16]. The M-H measurements shown in Fig. 2 were performed after the Mössbauer experiment and are in good agreement with results published earlier [14].

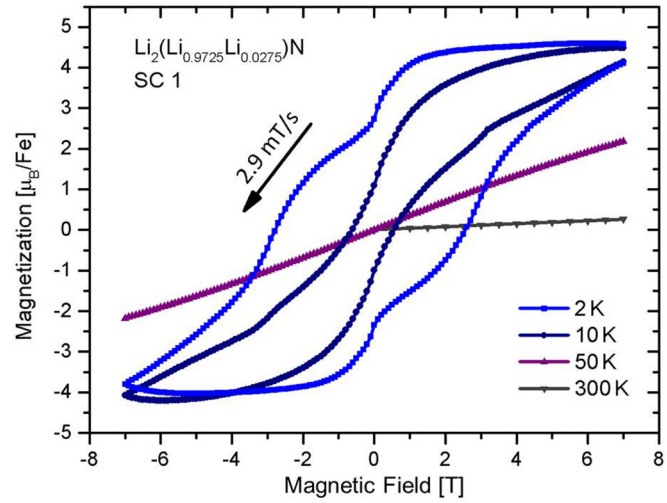

FIG. 2. Isothermal magnetization of $Li_2(Li_{1-x}Fe_x)N$ with $x = 0.0275$ (crystal SC 1) for $B_L \parallel c$ at various temperatures given in the plot.

B. Low-temperature ^{57}Fe Mössbauer spectroscopy at base temperature T_B

Mössbauer spectroscopy was performed at base temperature $T_B \leqslant 4$ K in zero field (ZF) on the crystals SC 1–4. At this temperature the lifetime of the electronic states exceeds that of the nuclear states. Therefore the hyperfine interactions are effectively stationary.

Figure 3 shows the ^{57}Fe Mössbauer measurement at T_B in ZF of SC 1–4. For SC 1, two Fe sites A (green) and B (red) are observed. The black line is given by the total transmission integral fitting function

$$T(v) = \int_{-\infty}^{\infty} L(E, v) e^{-\sigma(E) t_a} dE \qquad (2)$$

with the normalized Breit-Wigner resonance cross section $\sigma(E)$ depending on the energy E and an effective thickness $t_a = 2.39(10)$ reflecting a nonthin absorption limit. Therefore the black line represents the transmission integral fit whereas the lines for the sites A and B show the natural line $L(E, v)$. $T(v)$ is proportional to the line intensity of the recoil-free γ ray, a function of the absorber thickness, and v is the Doppler velocity, for details see Appendix. A thin absorber approximation is only valid for $t_a < 1$ and then is the line shape described by a Lorentzian $L(E, v)$ [21]. The fit is for SC 2–4 closer to the full thin absorption limit since the black line is replaced and shown by the green single Fe site A. The model used in Fig. 3 is the static crystal Hamiltonian $\hat{\mathcal{H}} = \hat{\mathcal{H}}_M + \hat{\mathcal{H}}_Q + \hat{\mathcal{H}}_Z$ assuming the same electric monopole $\hat{\mathcal{H}}_M$ and quadrupole interaction $\hat{\mathcal{H}}_Q$ for the two Fe sites A and B and independent Zeeman terms $\hat{\mathcal{H}}_Z$. We deduced an isomer shift of $\delta = 0.100(21)$ mm/s with respect to α-Fe at room

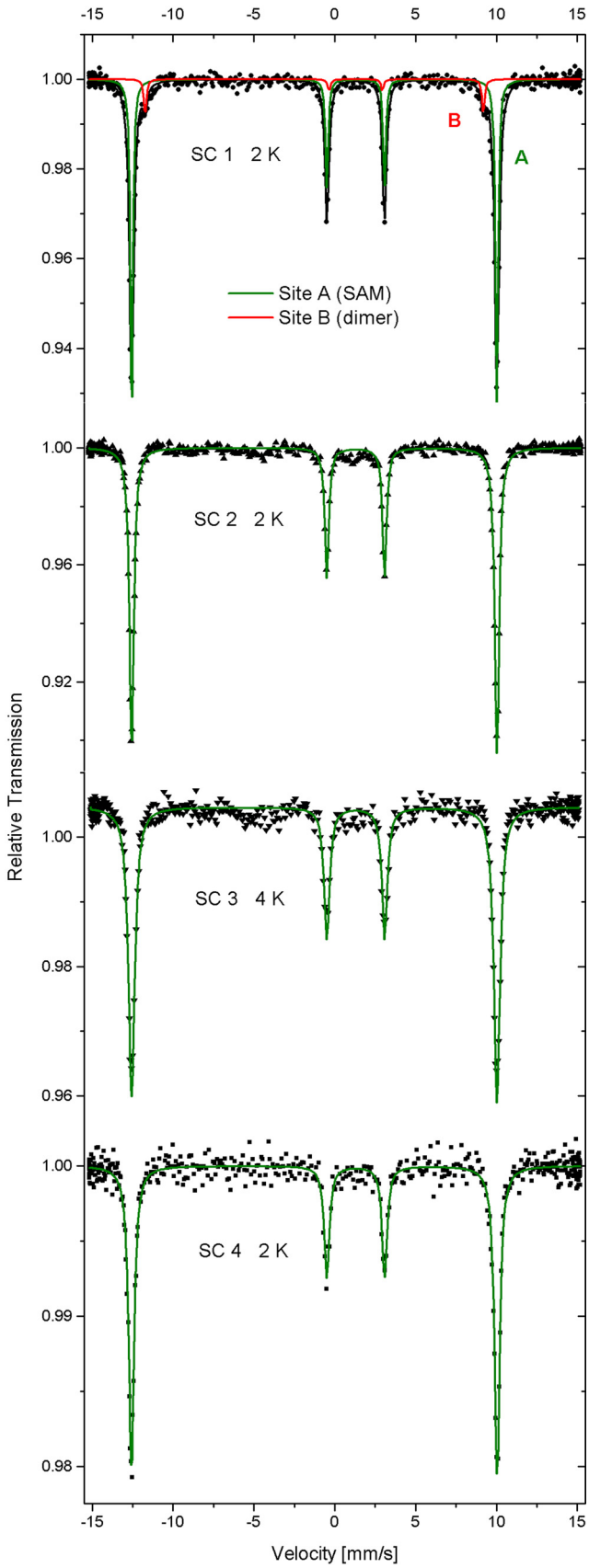

FIG. 3. Static Mössbauer spectra of $Li_2(Li_{1-x}Fe_x)N$ of the single crystals SC 1–4 as specified in Table I at base temperature $T_B \leqslant 4$ K in ZF.

temperature assuming a negligible second-order Doppler shift $\delta_{\mathrm{SOD}} \approx 0$ of the absorber at this temperature. The electric monopole interaction between the nuclear charge $Ze = 26e$ of ^{57}Fe with the charge number Z and the s-electron charge density $\rho_e(0) = -e|\psi(0)|^2_{A/S}$ at the nucleus is shifted by the energy E_A of the absorber material relative to the energy shift E_S of the source and leads to an effective energy shift

$$\delta = \frac{2\pi}{5} Ze^2 S(Z)\{|\psi(0)|^2_A - |\psi(0)|^2_S\}\left(R^2_{(e)} - R^2_{(g)}\right). \quad (3)$$

Here, $R^2_{(g)} = \langle r^2{}_{(g)}\rangle$ and $R^2_{(e)} = \langle r^2{}_{(e)}\rangle$ are the mean square values of the radii of the ^{57}Fe nucleus of the excited state (e) with nuclear spin $\frac{3}{2}$ and ground state (g) with nuclear spin $\frac{1}{2}$, respectively. $S(Z)$ is the dimensionless relativity factor which takes the spin-orbit coupling into account, e.g., for ^{57}Fe around $S(26) \approx 1.32$ or for neptunium $S(93) \approx 19.4$. These values vary slightly depending on the oxidation state. The monopole interaction $\hat{\mathcal{H}}_{\mathrm{M}}$ is given by a scalar $\hat{\mathcal{H}}_{\mathrm{M}} \equiv \delta + \delta_{\mathrm{SOD}}(T)$ as a function of the temperature. δ_{SOD} is the second-order Doppler shift and a direct consequence of the time dilation according to the relativity theory of the lattice dynamics. The γ-photon frequency ω_0 is shifted according to the transverse Doppler effect in the laboratory frame to

$$\omega = \omega_0 \frac{\sqrt{1 - v^2/c^2}}{1 - v\cos\alpha/c} \approx \omega_0\left(1 + \frac{v}{c}\cos\alpha - \frac{v^2}{2c^2}\right), \quad (4)$$

where v is the velocity of the nucleus, α the angle between the movement of the nucleus and γ-photon absorption and c the speed of light. The last term assumes $v \ll c$. This yields in the Debye approximation the expression

$$\delta_{\mathrm{SOD}} = -C\left[\Theta_D + 8T\left(\frac{T}{\Theta_D}\right)^3 \int_0^{\Theta_D/T} \frac{x^3 dx}{e^x - 1}\right] \quad (5)$$

with

$$C = \frac{9k_B E_\gamma}{16 M_{\mathrm{eff}} c^2}, \quad (6)$$

where M_{eff} is the effective mass. Using this expression to analyze the temperature dependence of the central shift in SC 1 yielded a Debye temperature of $\Theta_D = 315(8)$ K. For details see Appendix. To describe the electric quadrupole interaction $\hat{\mathcal{H}}_{\mathrm{Q}}$, e.g., SC 1 has a principle axis of the largest component of the EFG (electric field gradient) of $V_{zz} = -154.1(2)$ V/Å^2, denoted as usual,

$$|V_{zz}| \geqslant |V_{xx}| \geqslant |V_{yy}| \quad (7)$$

and the introduced asymmetry parameter

$$\eta = \frac{|V_{xx}| - |V_{yy}|}{|V_{zz}|} \leqslant 1. \quad (8)$$

This leads to the reduced quadrupole Hamiltonian

$$\hat{\mathcal{H}}_Q = \frac{eQV_{zz}}{4I(2I-1)}\left[3\hat{I}_z^2 - \hat{I}^2 + \frac{1}{2}\eta(\hat{I}_+^2 + \hat{I}_-^2)\right] \quad (9)$$

with the quadrupole moment Q and the raising and lowering spin operators $\hat{I}_\pm = \hat{I}_x \pm i\hat{I}_y$.

The pure quadrupole energy eigenvalues are given by

$$E_Q(m) = \frac{eQV_{zz}}{4I(2I-1)}[3m^2 - I(I+1)]\sqrt{1+\frac{\eta^2}{3}} \qquad (10)$$

with $I = 3/2$. The negative sign of $V_{zz} < 0$ corresponds to an elongation of the EFG charge distribution and an excess of negative charges in c-axis, the elongated case of the EFG ellipsoid [22]. The asymmetry parameter $\eta = 0$ assuming axial symmetry was used due to the hexagonal structure.

The magnetic hyperfine or Zeeman term $\hat{\mathcal{H}}_Z$ of the Hamiltonian $\hat{\mathcal{H}}_{\rm hf}$ is given by $\hat{\mathcal{H}}_Z = -g_N\mu_N\hat{\mathbf{I}}\cdot\hat{\mathbf{B}}$ with nuclear Landé factor g_N, the nuclear magneton $\mu_N = e\hbar/2m_pc$, the proton mass m_p and the magnetic field $\mathbf{B}$. Taking the scalar $|\mathbf{B}| = B$ and expresses $\hat{\mathcal{H}}_Z$ by the polar angle Θ and the azimutal angle Φ of $\mathbf{B}$ relative to direction of V_{zz} yields

$$\hat{\mathcal{H}}_Z = -g_N\mu_N B\left(\frac{\hat{I}_+e^{-i\Phi} + \hat{I}_-e^{+i\Phi}}{2}\sin\Theta + \hat{I}_z\cos\Theta\right). \qquad (11)$$

The values of the magnetic hyperfine fields for the two Fe subspecies converged to $B_A = 70.21(1)$ T and $B_B = 65.0(2)$ T. Site A is the dominant Fe site. Site B is only observed in SC 1 containing the highest Fe concentration with an intensity fraction of 5.9(3)%.

The two transitions

$$m = \pm\frac{1}{2} \rightarrow m = \pm\frac{1}{2} \qquad (12)$$

with $\Delta m = 0$ are not observed in the spectra of Fig. 3. The relative line intensities $W(\beta)$ depend on the polar texture angle β describing the direction of the incident γ ray with respect to the magnetic hyperfine field direction, $W(\beta) \propto \sin^2\beta$. For the analysis $\Theta = 0$ was taken. The angle β between the principle axis (largest component) V_{zz} of the EFG tensor and the γ beam was assumed to be an identical fit parameter for the monomer site A and the dimer site B. The resulting value $\beta = 0$ proves that the magnetic hyperfine field and V_{zz} are aligned parallel to the c axis. The result is the observed ratio of the spectral line intensities of 3:0:1:1:0:3. Figure 4 shows the geometry of the hyperfine interactions with respect to the linear N-Fe-N bond and with respect to the γ beam.

No indications for Fe site B are observed in SC 2 as well as in SC 3 and SC 4. The green line is the fit of the model of the static crystal Hamiltonian $\hat{\mathcal{H}}_{\rm hf}$ with an isomer shift $\delta = 0.119(20)$ mm/s and a principle axis of the EFG of $V_{zz} = -154.2(4)$ V/Å^2. The asymmetry parameter is assumed to be $\eta = 0$. The fit yielded a magnetic hyperfine field $B_A = 70.24(1)$ T parallel to V_{zz} of the EFG tensor and parallel to the γ beam as well. Table II shows the obtained hyperfine parameters of SC 1–4 and the calculated mean values of $\bar{V}_{zz}$, $\bar{B}_A$, $\ln\bar{\nu}_0$, and $\bar{E}_A$. The hyperfine parameters are nearly concentration-independent. The absolute values of the magnetic hyperfine fields B_A and B_B are above typical spin-only values in solid state systems and can be understood in terms of a strong unquenched orbital contribution. The analysis to obtain the fluctuation rate parameters $\ln\bar{\nu}_0$ and $\bar{E}_A$ of the Arrhenius temperature dependence is described in Appendix E.

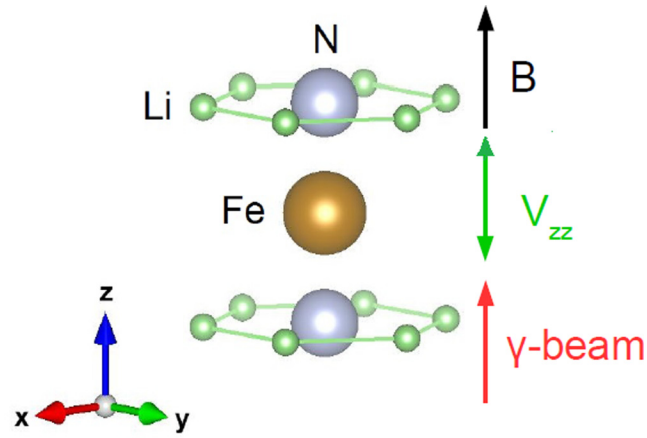

FIG. 4. Geometry of hyperfine interactions as obtained from the static hyperfine Hamiltonian with the magnetic hyperfine field B, the γ beam and the strongest component V_{zz} of the EFG tensor parallel to the crystallographic c axis (N-Fe-N bond), which is also the magnetic easy axis, i.e., the quantization axis (z axis) discussed in the spin Hamiltonian analysis below.

C. Zero-field ^{57}Fe Mössbauer spectroscopy for $T_B < T < 300$ K

Above 50 K, the ^{57}Fe nucleus interacts with a fluctuating magnetic hyperfine field. Figure 5 shows representative spectra between 60 and 200 K of SC 1 with $x = 2.75\%$. In the following we will only consider Fe site A, site B is neglected in this analysis. The fit represents a Blume dynamic line shape model in the presence of quadrupole hyperfine interactions for two states, described by absorption cross section

$$\sigma = -\frac{\sigma_a\Gamma_0}{2}\mathrm{Im}\sum_\alpha \mathrm{Sp}\left(\hat{V}_\alpha\,\langle W|\,\hat{\mathbf{A}}^{-1}(\omega,\Theta)\,|1\rangle\,\hat{V}_\alpha^+\right). \qquad (13)$$

Here, $\hat{V}_\alpha$ is the operator of hyperfine interactions of the γ beam with polarization α and the nucleus, σ_a the effective absorber thickness and $\langle W|$ and $|1\rangle$ as described by Chuev and therein [23]. The superoperator

$$\hat{\mathbf{A}}(\omega,\Theta) = \tilde{\omega} + i\Gamma_0/2 - \hat{\mathbf{L}}(\Theta) + i\hat{\mathbf{P}} \qquad (14)$$

is defined by the Liouville operator of hyperfine interactions $\hat{\mathbf{L}}(\Theta)$, the resonance transition energy E_0 is given by the corresponding frequency $\tilde{\omega} = \omega - E_0/\hbar$, Γ_0 the width of the excited nuclear level and $\hat{\mathbf{P}}$ the matrix of hyperfine transitions [20,23–25].

The initial conditions for the analysis are identical to the static case at 2 K. A two level relaxation model was

TABLE II. Hyperfine parameters V_{zz}, B_A as well as the Arrhenius parameters $\ln\nu_0$ and E_A of SC 1-4. The errors represent standard deviations obtained during linear regression.

	V_{zz} (V/Å^2)	B_A (T)	E_A (K)	$\ln(\nu_0$ [MHz])
SC 1	−154.1(2)	70.21(1)	552(26)	12.36(32)
SC 2	−154.2(4)	70.24(1)	563(12)	12.48(11)
SC 3	−154.0(2)	70.23(1)	581(12)	12.65(11)
SC 4	−154.0(6)	70.30(2)	552(44)	12.08(49)
Mean value	−154.0(1)	70.25(2)	570(6)	12.64(7)

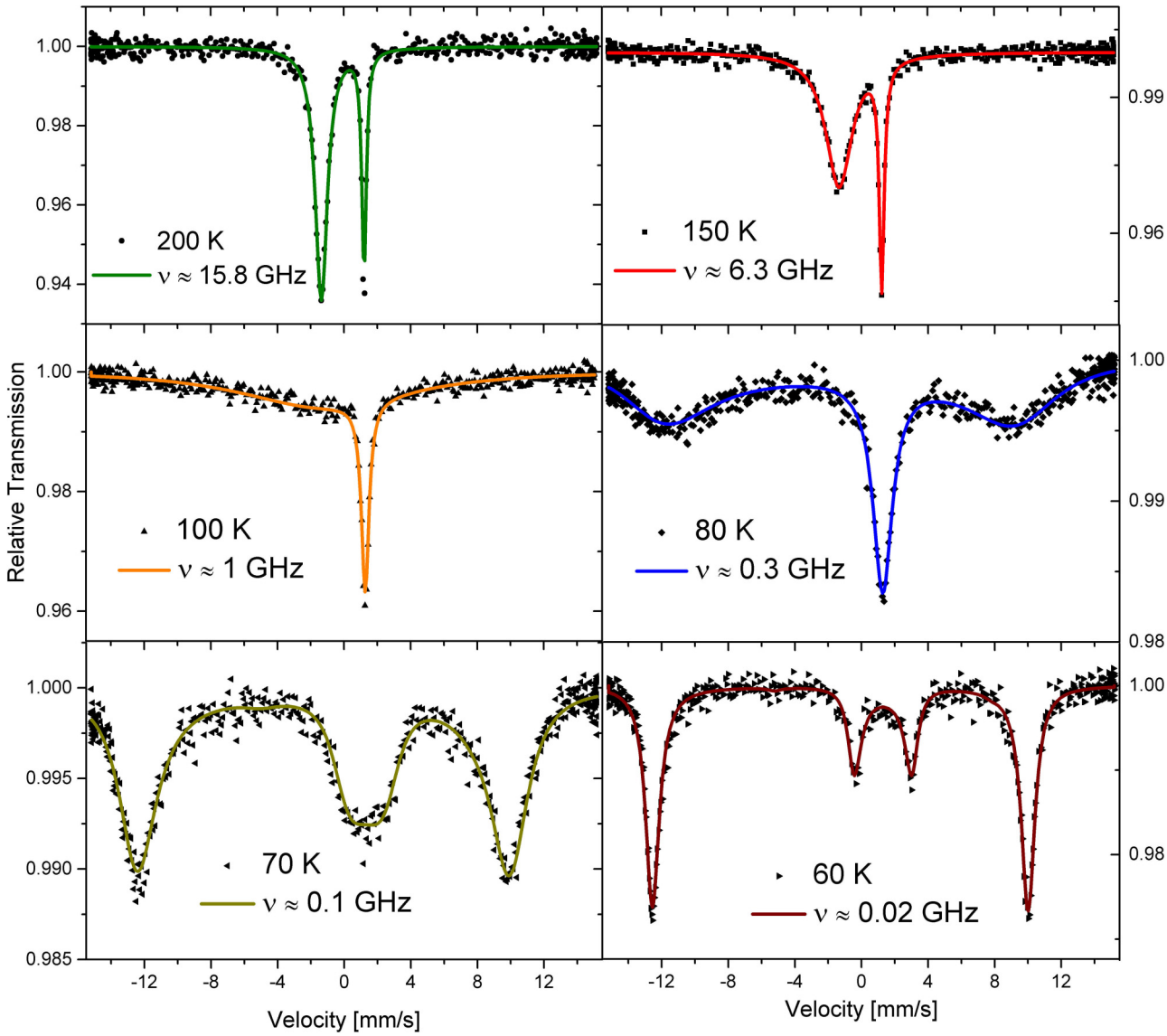

FIG. 5. Mössbauer spectra of SC 1, $Li_2(Li_{1-x}Fe_x)N$ with $x = 2.75\%$. Lines show a two level Blume model fluctuation spectrum analysis [20]. The magnetic hyperfine field fluctuates between $+B_A$ and $-B_A$ with the frequency ν. B_A in this model is assumed to be parallel to V_{zz} and to the γ beam.

used taking into account an electronic spin reversal process. The magnetic hyperfine field fluctuates with the fluctuation frequency ν between the two values $+B_A$ and $-B_A$. Above 60 K the spectral lines begin to broaden due to the fluctuations, see Fig. 5. With increasing ν at 70 K, the two internal lines collapse first yielding a singlet at 100 K. At 150 K and above, the left resonance line of the quadrupole doublet, which is expected to appear in the fast relaxation limit $\nu \to \infty$, results from the collapse of the external lines [26]. The Arrhenius parameter E_A and $\ln \nu_0$ are obtained by an Arrhenius analysis

$$\ln \nu = \ln \nu_0 - \frac{E_A}{k_B}\left(\frac{1}{T}\right) \tag{15}$$

of the extracted fluctuation frequencies $\ln \nu$ of SC 1–4. In this analysis, the values of ν for $T < 50$ K are not considered since these value reflect the lower bound of the fluctuation rate which the Mössbauer spectra analysis can resolve. This yielded a thermal activation barrier of $E_A = 552(26)$ K and $\ln \nu_0 = 12.36(32)$ GHz for SC 1. The fluctuation frequency ν of Fe site A is essentially concentration-independent in SC 1–4. Table II shows the Arrhenius plot fit parameter of SC 1–4, for details see Appendix.

D. ^{57}Fe-Mössbauer spectroscopy in transverse magnetic fields B_T

Here we present the results of Mössbauer spectroscopy experiments under applied transverse magnetic fields B_T up to 5 T as illustrated in Fig. 6. Therefore the field is applied perpendicular to the quantization axis of the Fe spins which is determined by the direction of the magnetic hyperfine field at the Fe nucleus, i.e., the crystallographic c axis. In this geometry, an increasing field B_T leads to an increasing mixture of the S_z eigenstates of the electronic spins and an increasing fluctuation rate of the magnetic hyperfine field is expected supported by a theoretical treatment based on

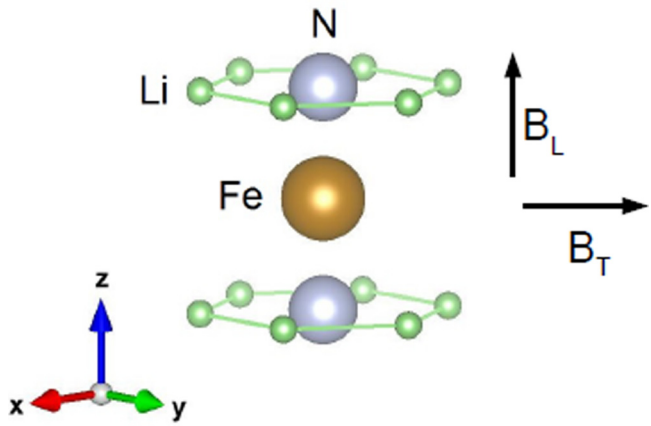

FIG. 6. Illustration of applied magnetic fields perpendicular (B_T) or parallel (B_L) to the quantization axis (z axis) which is the crystallographic c-axis.

the minimal spin Hamiltonian of a single-ion in the next section. These experiments were performed on sample SC 1. Figure 7 shows four typical Mössbauer spectra in different transverse magnetic fields (TF) up to 5 T. The experimental data clearly reveal an increase of the fluctuation frequency ν with increasing field strength. The temperature and field range for these experiments was chosen such that the slowly fluctuating magnetic hyperfine field of ≈70 T can be regarded as the dominant hyperfine interaction with the ^{57}Fe nuclei and the Blume model of axial fluctuations of the magnetic hyperfine field described in the former subsection can be used for the quantitative analysis (solid lines in Fig. 7). For higher fields the vector sum of the external field and the internal magnetic hyperfine field must be considered.

At $T = 70$ K, ν has increased in 1 T by a factor 2 and in 5 T by a factor 8. This documents a strong transverse field sensitivity. The dependence of the fluctuation frequency ν on the transverse magnetic field B_T and temperature T is investigated in detail for SC 1. Figure 8 shows the logarithmic frequency $\log_{10}$ as a function of the inverse temperature $1/T$ for different transverse external fields and Fig. 9 shows the logarithm of ν as a function of the transverse magnetic field for different temperatures.

The used fit function is discussed in the spin-Hamiltonian part below and in the Appendix. In Fig. 8, at low temperatures $1/T > 0.01$ K^{-1}, a pronounced field-induced non-linear deviation from the zero-field Arrhenius line is observed. For high temperatures $1/T < 0.01$ K^{-1} the data converge to the zero-field Arrhenius line, i.e., the temperature-induced fluctuations are dominant. This is also seen in Fig. 9: the change of ν with increasing B_T is enhanced by lowering the temperature. Note that for the lowest temperatures (30 and 40 K) the determined fluctuations rates are close to the lower bound of the frequency window of the Mössbauer method due to the effective time window.

To describe the change of the spin fluctuation rates induced by the applied transverse magnetic field, we considered a simplified perturbation proportional to $B_T J_x \equiv B_T(J_+ + J_-)/2$. Such a term can mix the states with different J_z, however with one difference from the O_6^6 processes discussed in section III F

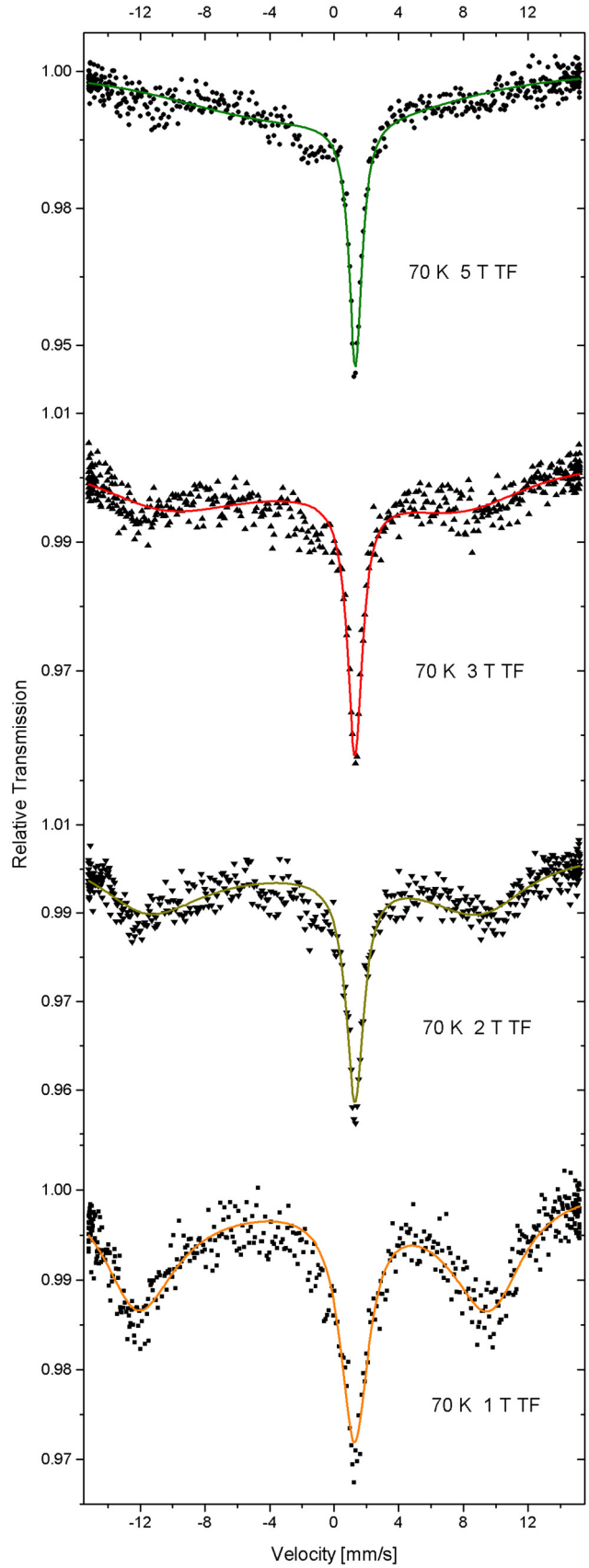

FIG. 7. Mössbauer spectra of SC 1 in various transverse magnetic fields B_T at 70 K. The corresponding ZF measurements are shown in Fig. 5.

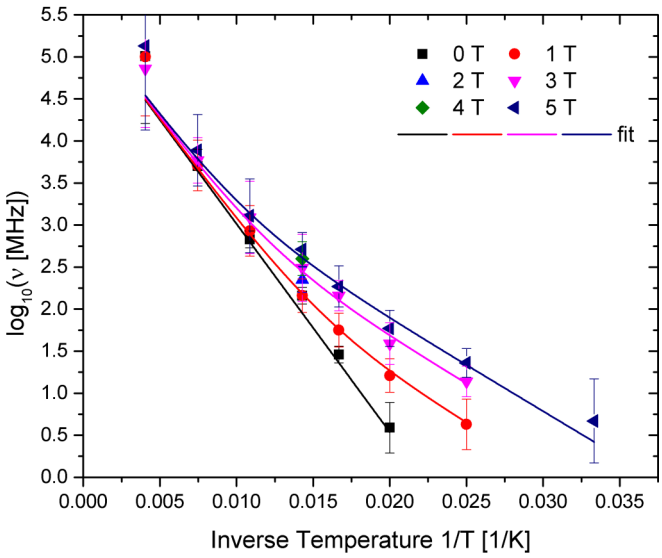

FIG. 8. Dependence of the spin fluctuation rate on temperature for $Li_2(Li_{1-x}Fe_x)N$ with $x = 2.75\%$, SC 1, in transverse magnetic fields B_T. The solid line fitting function is described in the text.

below, namely, $\Delta J_z = 1$. We have described our experimentally observed fluctuation rate data by a function linear in B_T. The data can be described with the phenomenological model function

$$\nu(T, B_T) = \nu_0 e^{-\frac{\Delta_1}{T}} + \xi B_T e^{-\frac{\Delta_2}{T}}. \quad (16)$$

The first term describes the field-independent temperature-activated Arrhenius contribution observed in the ZF experiments using $\bar{\nu}_0$ and $\Delta_1 = \bar{E}_A/k_B$ (see Fig. 16 and black >line in Fig. 8). The second term describes the increase of ν due to the transverse field scaling linear with B_T. In a global fit $\bar{\nu}_0$, ξ and Δ_i are constant parameters. The result is $\xi = 2332(995)$ MHz/T and $\Delta_2 = 251(20)$ K. We associate

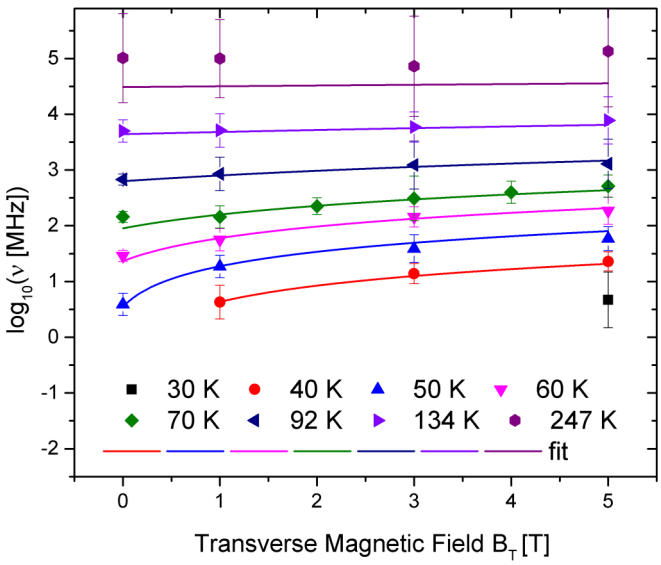

FIG. 9. Dependence of the spin fluctuation rate on the transverse magnetic field for $Li_2(Li_{1-x}Fe_x)N$ with $x = 2.75\%$, SC 1, for various temperatures. The solid line fitting function is described in the text.

this relaxation process with a second Orbach process which is observed by ac susceptibility below 30 K (see Fig. 13). The applied transverse field increases the attempt frequency so that it becomes detectable within the Mössbauer frequency window.

E. ^{57}Fe-Mössbauer spectroscopy in longitudinal magnetic fields B_L

^{57}Fe-Mössbauer spectroscopy measurements were performed with applied longitudinal magnetic fields (LF) at 100 K up to 3 T with the γ beam parallel to the applied field parallel to the c-axis of the crystal as illustrated in Fig. 6. Therefore the field is applied parallel to the quantization axis of the Fe spins. It's main impact is to modify the energy levels of the J_z eigenstates.

Figure 10 shows the ^{57}Fe Mössbauer measurements at 100 K up to 2 T longitudinal magnetic field (LF). The measurements at 0.5 and 1 T show an increase of the linewidth of the central absorption line compared to the ZF spectrum. The spectra at 2 T clearly reveals a splitting into two lines corresponding to two different fluctuation rates. The analysis model to describe the LF spectra is the Blume two-state spin reversal fluctuation model between the states with hyperfine fields $B_h = B_A + B_L$ and $B_h = -B_A + B_L$. Since the Zeeman interaction will lift the degeneracy between the "spin up" and "spin down" transitions two different fluctuation frequencies ν_{up} describing the frequency to flip the spin into longitudinal magnetic field direction and ν_{down} to flip it against the applied field direction are considered. The population of the two states are assumed to be the same as shown by the equal central line intensities at 2 T in Fig. 10. Note that a small static external field at the ^{57}Co-source caused by the Helmholtz magnet leads to a slight increase of the linewidth (0.24(2) mm/s at 2 T). Figure 11 shows the deduced frequencies $\log_{10}\nu_{up}$ and $\log_{10}\nu_{down}$ as a function of the longitudinal magnetic field B_L. The observed change of the fluctuation rate is one order of magnitude smaller than in the case of applied transverse fields. The data show a linear dependence of $\log_{10}\nu_{up}$ and $\log_{10}\nu_{down}$ as a function of B_L up to 3 T. We clearly observe an asymmetry of the observed positive and negative frequency changes, i.e., a stronger increase of $\nu_{up}(B_L)$ than decrease of $\nu_{down}(B_L)$. This cannot be explained by the Zeeman-induced decrease of the energy differences for the transition $J_z = -7/2 \rightarrow J_z = 5/2$ and increase of the energy difference for $J_z = 7/2 \rightarrow J_z = -5/2$ since these changes are of equal absolute value. The experimental slopes are given by $0.084(5)\log_{10}$[MHz]/T for ν_{up} and $-0.015(3)\log_{10}$[MHz]/T for ν_{up}, respectively. The theory curves (orange lines) shown in Fig. 11 will be discussed in Sec. III G.

F. Effective single-ion $J_{eff} = 7/2$ Hamiltonian calculation of spin dynamics

A striking result of the temperature and transverse magnetic field dependent Mössbauer spectroscopy is that the activation energy scale for thermal fluctuations of the individual electronic Fe spins $E_A \approx 570$ K is two orders of magnitude larger than the Zeeman energy $g_t \mu_B B_x S_x \sim 5$ K which is needed to induce similar changes of the fluctuation rate.

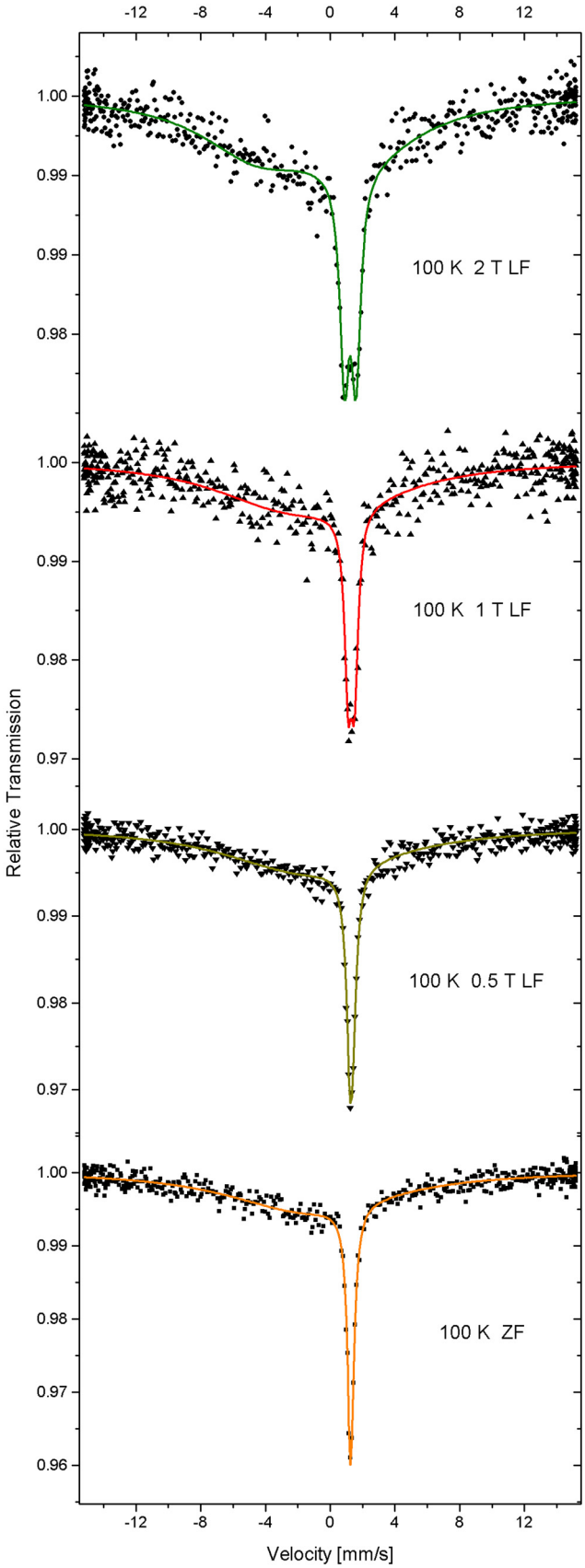

FIG. 10. Mössbauer measurements of SC 1 at 100 K in ZF and in applied longitudinal magnetic fields B_L of 0.5 T, 1 T and 2 T.

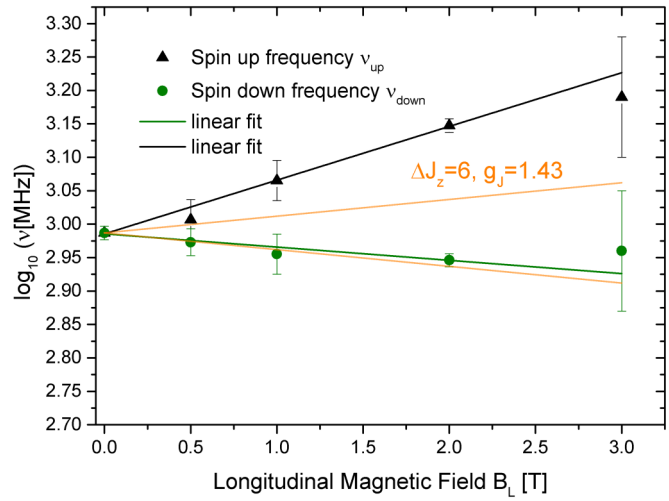

FIG. 11. The fluctuation frequencies ν_{up} and ν_{down} as a function of the applied longitudinal magnetic field B_L. The dashed orange lines describe the expected values of $\nu_{up}(B_L)$ and $\nu_{down}(B_L)$ for Zeeman contributions to the energy levels of the $J = 7/2$ Fe ions and $\Delta J_z = \pm 6$, for details see Sec. III G.

Moreover it is important to note, that the low-temperature longitudinal magnetic field magnetization data on this system presented in Fig. 2 also reveal an energy scale for longitudinal magnetic field induced system changes of the order of 1 to 5 K from the appearance of level crossing induced magnetization steps at $\mu_0 H_z = 0.15,\ 0.55$, and 3 T.

For a qualitative understanding of the transverse magnetic field and temperature dependence of the spin fluctuation frequency ν we present a calculation of the spin dynamics using a single-ion spin Hamiltonian model. We demonstrate that an axial anisotropy of energy scale $D \ll 570$ K, consistent with the Zeeman response of the system, can indeed give rise to an effectively two orders of magnitude larger energy barrier for thermal fluctuations. Moreover, qualitatively, the obtained results can be extended to a broad class of SAM and SMM by the introduced effective mixing term.

We consider the single-ion properties of Fe ions in $Li_2(Li_{1-x}\ Fe_x)N$. Considering spin-orbit interaction and the hexagonal point symmetry of the Fe site (1*b* Wyckoff site, point symmetry $6/mmm$ [11]), the crystalline electric field yields the single-ion magnetic anisotropy $\mathcal{H}_{an} = B_2^0 O_2^0 + B_4^0 O_4^0 + B_6^0 O_6^0 + B_6^6 O_6^6$, where O_n^m are Stevens' operators, and B_n^m are the parameters of the magnetic anisotropy [27–29]. The Fe ions in Li_3N can be either Fe^+ (which, according to Hund's rules have the lowest multiplet with $S = 3/2$, $L = 3$, and $J = 9/2$), or Fe^{2+} (with $S = 2$, $L = 2$, and $J = 4$). For diluted Fe in α-Li_3N, however, we can apply the arguments used in Refs. [12,30], where a ground state of $|M_L = -2, M_S = -3/2\rangle$ was proposed. The oxidation state Fe^{1+} d^7 is consistent with our obtained hyperfine parameters, see discussion. The arguments, namely, the strong uniaxial anisotropy of the hexagonal lattice (due to O_2^0, O_4^0 and O_6^0 operators, which distinguish only $z \parallel c$ axis) lifts the degeneracy, and only $L = 2$ states are coupled with $S = 3/2$ for Fe^+ in α-Li_3N. It yields the effective total moment $J_{\text{eff}} = 7/2$. The splitting of the Mössbauer lines (see Fig. 10) also confirms

that assumption: The splitting is too large for pure spin states $S = 3/2$ or $S = 2$. In what follows, we call J a pseudo-spin and drop the index "eff" for simplicity. However, qualitatively, the calculated results below are independent of the detailed value of J.

The most important part of the Hamiltonian $\mathcal{H}_{an}$ can be written as $\mathcal{H}_{an} \approx -DJ_z^2$, where D is the parameter of the magnetic anisotropy. We can conclude from the magnetization experiments and the spin-reversal Blume model with axis c $||B_A||V_{zz}$, that we deal with "easy-axis" magnetic anisotropy, $D > 0$. Consider the Hamiltonian of the Fe ion in the external magnetic field $B_z = B_L$, directed along the "easy" axis, namely $\mathcal{H}_0 = -DJ_z^2 - g_l\mu_B B_z J_z$, where μ_B is the Bohr magneton, and g_l is the (longitudinal) z-component of the effective g tensor. The levels of that Hamiltonian cross each other at several values of B_z, depending on the value. The only Stevens' operator from $\mathcal{H}_{an}$, which does not commute with J_z, and, hence, which can mix states with different values of J_z and lift the degeneracies at the crossover points, is $O_6^6 \equiv (J_+^6 + J_-^6)$, where $J_\pm = J_x \pm iJ_y$. Such a mixing is the crucial point for the quantum tunneling [31]. Notice that according to standard quantum mechanics in the basis with diagonal action of the operator J_z the eigenstates of O_6^6 for $J = 3/2$ and $J = 2$ are zero. The operator O_6^6 corresponds to the processes with $\Delta J_z = 6$, hence connecting the states $J_z = -7/2$ with $J_z = 5/2$, and $J_z = -5/2$ with $J_z = 7/2$.

Unfortunately, the explicit results for the relaxation rate due to quantum tunneling cannot be realized for O_6^6 because of the numerical effort. Therefore, to mimic the action of the operator O_6^6 we consider a more simplified perturbation related to the transverse magnetic field, for example, $J_x \equiv (J_+ + J_-)/2$. Such a term also can mix the states with different J_z, however with one difference from the O_6^6 processes, namely $\Delta J_z = 1$. This substitution of O_6^6 by J_x, while giving the opportunity to obtain a qualitative agreement with the results of our experiments, still cannot give a full quantitative description of $Li_2(Li_{1-x}\,Fe_x)N$.

Summarizing, we consider, an effective Hamiltonian, which permits quantum tunneling in $Li_2(Li_{1-x}\,Fe_x)N$. It has the form

$$\mathcal{H} = -DJ_z^2 - g_t t\mu_B B_x J_x - g_l\mu_B B_z J_z, \tag{17}$$

where g_t is the value of the effective g-tensor in the plane, transverse to the easy axis. Note that B_x can include not only the effective field, introduced to mimic the action of the O_6^6, but also internal (dipole) or external magnetic fields applied transverse to the z axis, i.e. perpendicular to the crystallographic c axis. According to Refs. [31,32] the lowest $(2J + 1)$ eigenvalues and eigenfunctions of that Hamiltonian coincide with those of the discrete spectrum of a quantum particle in the effective potential

$$U = \frac{DB^2}{4}\left[\sinh(x) - \frac{C}{B}\right]^2 - \frac{DB}{2}(2J+1)\cosh(x), \tag{18}$$

where $B = g_t\mu_B B_x/D$ and $C = g_l\mu_B B_z/D$. The spin quantum tunneling in that approach is totally equivalent to the tunneling of that quantum particle between the minima of the potential U. The tunneling rate can be calculated using the Euclidean version of dynamical equations, using dynamics of instantons of the Eulcidean action, i.e., solitons, connecting two minima of the potential U with each other [33]. Consider the range of the field values, limited by the region $[B^{2/3} + C^{2/3}]^{3/2} < 2J + 1$, in which the potential U has two minima (the lowest minimum is related to the stable state, and the highest one to the metastable state). The energy barrier between the minima is finite, hence there exists a probability for the metastable state to decay due to the quantum tunneling. It is possible to calculate the values of the relaxation rate due to the quantum tunneling [31,32], expanding the expression for U near the position of the metastable minimum. The decay rate is determined by the analytic continuation of the energy value to the complex plane. Analyzing the results obtained this way, we conclude that two regimes, $T_0 \leqslant T \leqslant T_1$, and $T \geqslant T_1$, where $T_0 = D\sqrt{a}/\pi k_B$, and $T_1 = 2D\sqrt{a}/\pi k_B$ can be related to the conditions of our experiments with $Li_2(Li_{1-x}\,Fe_x)N$. Here and below we use the notations

$$\begin{aligned} a &= \frac{3^{1/2}}{2^{3/2}} BC^{1/3}(2J+1)^{2/3}\delta^{1/2}\,, \\ b &= \frac{1}{12} B^{4/3}C^{1/3}(2J+1)^{1/3}\,, \\ \delta &= 1 - \frac{\left(B^{2/3} + C^{2/3}\right)^{3/2}}{2J+1}\,. \end{aligned} \tag{19}$$

For $T_0 \leqslant T \leqslant T_1$, i.e., at low temperatures for our experiment, the relaxation rate can be approximated as, according to Ref. [31],

$$\begin{aligned} \hbar\gamma_1 = D\frac{\sqrt{a}\sinh(D\sqrt{a}/k_BT)}{\pi\sin(D\sqrt{a}/k_BT)} \\ \times \exp\left[-4Da^3/27b^2k_BT\right]. \end{aligned} \tag{20}$$

On the other hand, for higher temperatures $T \geqslant T_1$, the relaxation rate is

$$\hbar\gamma_2 = D\frac{\sqrt{a}}{\pi}\exp\left[-4Da^3/27b^2k_BT\right]. \tag{21}$$

This higher-temperature behavior of the relaxation rate caused by the quantum spin tunneling is similar to the Orbach relaxation [34], i.e., it has the Arrhenius form. Notice that the "true" quantum spin tunneling-induced relaxation rate exists only at $T = 0$ [31,32].

Given that the pre-expontial factor, ν_0, obtained from Mössbauer spectroscopy is temperature-independent [as the pre-exponential factor in Eq. (21)], the most essential regime for our experiments with $Li_2(Li_{1-x}\,Fe_x)N$ is the region with $T \geqslant T_1$. We see that the relaxation rate γ_2 follows an Arrhenius law in the temperature dependence, $\gamma_2 = \nu_0\exp(-E_A/k_BT)$ with the prefactor ν_0 and the activation energy E_A determined as

$$\begin{aligned} \nu_0 &= \frac{D\sqrt{a}}{\pi\hbar} \sim B_x^{1/2}B_z^{1/6}\delta^{1/4}\,, \\ E_A &= \frac{4Da^3}{27b^2} \sim (B_xB_z)^{1/3}\delta^{3/2}\,. \end{aligned} \tag{22}$$

In detail,

$$E_A \approx 4.89B^{1/3}C^{1/3}(2J+1)^{4/3}\delta^{3/2}, \tag{23}$$

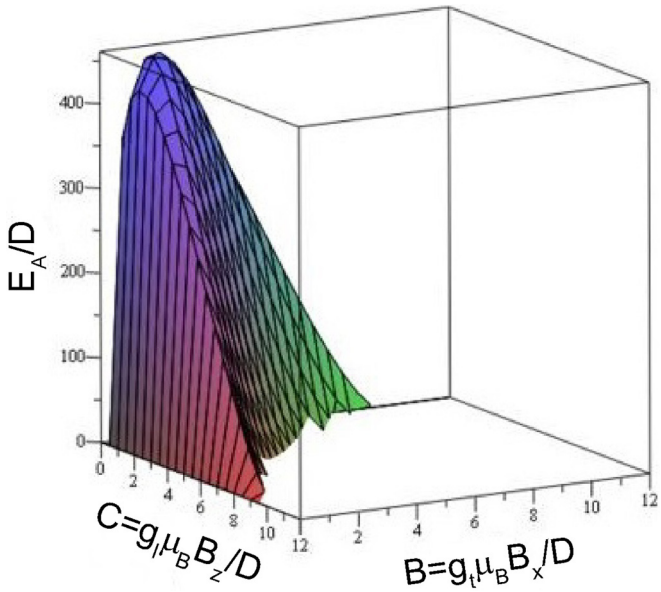

FIG. 12. The dependence of the activation energy E_A for the relaxation rate γ_2 on the longitudinal B_z and transverse B_x.

where the factor $(2J+1)^{4/3}$ is the dominant scaling factor for $J > 3/2$.

Note that we cannot use the limits $B_x \to 0$, and $B_z \to 0$ in the expression for the relaxation rate caused by the spin tunneling, because the latter is absent there: without B_z there is no crossover, and without B_x there is no lifting of the degeneracy of crossover points. However, we can evaluate the field dependence of the activation energy, not taking into account the limiting cases $B_x \to 0$ and $B_z \to 0$. A weak effective tilted magnetic field can originate, e.g., from the long-range magnetic dipole-dipole interaction in the mean field approximation. We also suppose that the region of applicability of the results can be expanded to all $\delta < 1$, which implies the difference between the potential U and its expansion near the position of the metastable state being small (this difference produces higher-order quantum corrections). The result is shown in Fig. 12 for $J = 7/2$. We see that for very small but finite values of the components of the external magnetic field the activation energy is much larger than the value of the magnetic anisotropy D. It explains the observation of the giant activation energy for the relaxation rate in our Mössbauer studies of $Li_2(Li_{1-x}\ Fe_x)N$. Furthermore, we see that the application of the external field of the order of $(2J+1)D$ reduces drastically the value of the activation energy.

Now we can compare the transverse field dependence of the relaxation rate, extracted from Mössbauer experiments in $Li_2(Li_{1-x}\ Fe_x)N$ with the calculated one. In Fig. 13(a), the logarithm of the relaxation rate γ_2 is plotted as a function of the applied transverse field B_x at $g_l \mu_B B_z = 0.001$ for $J = 7/2$ and several values of the temperature. To have better agreement with experiment we have to add the constant $g = 3.5$ to $\log_{10}(\gamma_2)$, which implies additional sources of relaxation that are temperature- and magnetic field-independent. Figure 13(b) shows the logarithm of the relaxation rate γ_2 as a function of the inverse temperature, $1/T$, for several values of the transverse external magnetic field B_x. We see that the

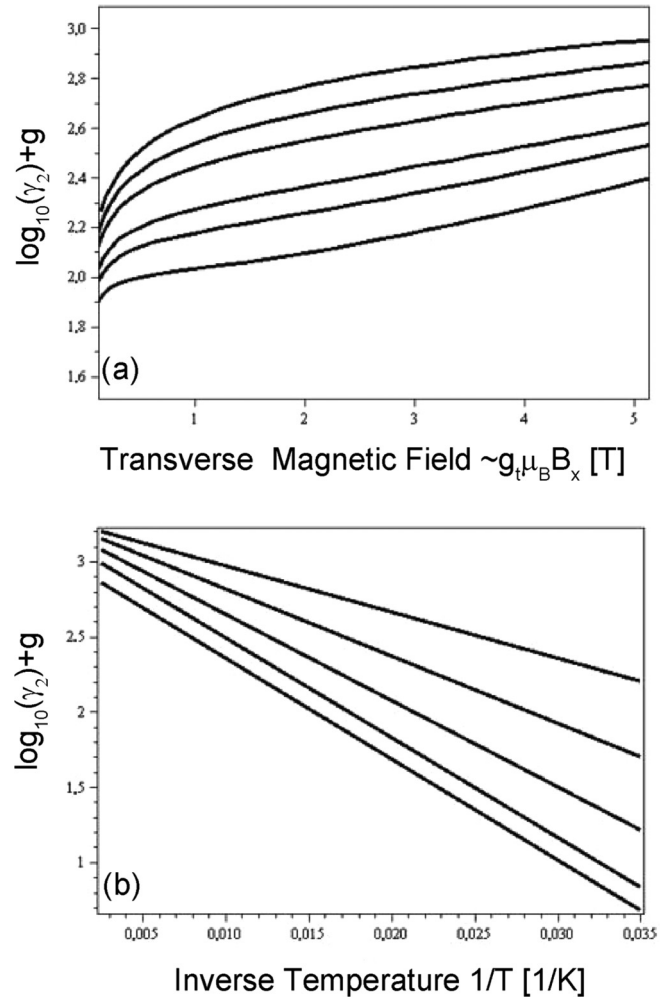

FIG. 13. (a) The dependence of the logarithm of the relaxation rate γ_2 on the transverse field B_x for several values of T. From top to bottom: $T = 247$, 134, 92, 60, 50 and 40 K. (b) The dependence of the logarithm of the relaxation rate γ_2 on the inverse temperature $1/T$ for several values of the transverse field B_x. From bottom to top: $B_x = 1$, 2, 3, 4, and 5 T.

general tendency is well described by our simplified theory, while there is no quantitative agreement.

We conclude that this single-ion theory, based on the spin properties of Fe impurities, which at low energies produce quantum spin tunneling, well reproduces the most dramatic feature of dynamical experiments in $Li_2(Li_{1-x}\ Fe_x)N$: the giant value of the activation energy in the Arrhenius law for the temperature dependence of the relaxation rate, and much smaller values of the external magnetic field, which drastically change that relaxation rate.

G. Zeeman analysis of spin dynamics in longitudinal fields B_L

The splitting of the resonance line in longitudinal fields (Fig. 10) can be understood as a consequence of the Zeeman term in the effective spin Hamiltonian. For $B_z = 0$ the relevant relaxation processes with $\Delta J_z = \pm 6$ introduced in the last section are equivalent. However, a finite longitudinal field $B_z = B_L$ removes the degeneracy of the $\pm J_z$ energy levels

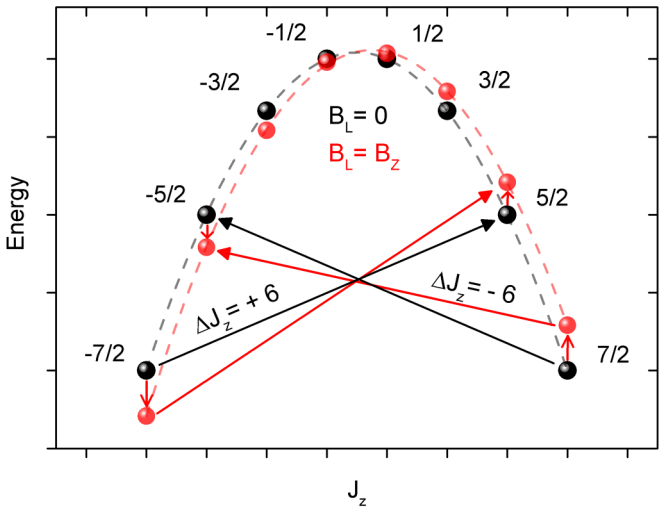

FIG. 14. Illustration of the transitions between $J_z = -7/2$ and $J_z = 5/2$ and $-7/2$ to $+5/2$. The energy levels J_z are shifted in LF (red points) leading to different transition energies according to the Zeeman energy $E_Z \sim J_z B_Z$.

via Zeeman interaction. The values of the energy differences between the states $J_z = -7/2$ and $5/2$, and between the states $J_z = -5/2$ and $7/2$ become nonequal (see Fig. 14).

To calculate these energy differences we need to specify the longitudinal g-factor g_l. Here, we model the complex many electron state of the Fe ions including strong spin-orbit interaction by a simplified $J = 7/2$ system with a fixed Landé g-factor value of $g_l = 1.43$ (based on $L = 2$ and $S = 3/2$, see Appendix) for both, the ground state (assumed to be $J_z = \pm 7/2$) and the excited state (assumed to be $J_z = \pm 5/2$). This choice of g_l leads to an effective paramagnetic moment $\mu_{\text{eff}} = g_l \mu_B \sqrt{J(J+1)} \approx 6.15 \mu_B$ which is consistent with the experimental value.

According to the Arrhenius law, the change of the spin fluctuation rate with respect to its ZF value can be calculated according to

$$\nu(B_L)/\nu(B_L = 0) = \exp\left(\frac{E_Z}{kT}\right). \tag{24}$$

Here, $E_Z = \pm g_l \mu_B \Delta J_z B_L$ is the Zeeman term with the transition rule $\pm \Delta J_z$. The $\pm$-sign corresponds to the positive and negative branches in Fig. 11. To calculate the Zeeman induced change of the spin fluctuation rate $\nu(B_L)$, we use $\Delta J_z = 6$ according to the hexagonal symmetry. The resulting slope of ν versus B_L is

$$\frac{\Delta \log_{10} \nu}{\Delta B_L} \approx \pm 0.025/\text{T}. \tag{25}$$

The results of this calculation are included in Fig. 11 as orange lines. The calculated values for $\nu(B_L)$ are below the experimental results for the branch $\nu_{\text{up}}(B_L)$ as well as the branch $\nu_{\text{down}}(B_L)$. This is expected since a second contribution stemming from the B_L dependence of the $B_6^6 O_6^6$ term in the crystal field spin Hamiltonian is not included in this model. Such a term is always positive, linear in B_L and identical for both branches. Therefore the Zeeman contributions to ν_{up} and ν_{down} must be located below the experimental values, ideally shifted by identical values with respect to the experimental values. The latter is not fulfilled (cf. Fig. 11), however increasing the absolute value of both slopes [Eq. (25)] by ≈80% would lead to such a situation. Note that a correction of this size is feasible since from all experiment performed on $Li_2(Li_{1-x}Fe_x)N$ so far we cannot determine the ground state and excited state values of J_z exactly. Moreover, also the longitudinal g-factors g_l for both states in this effective spin Hamiltonian approach can be modified strongly due to the subtle interplay of the crystal electric field with the spin-orbit coupling in this $3d^7$ state. A more realistic many-body electronic structure calculation is needed to calculate the effective crystal field energies as well as the longitudinal and transverse g-factors of the ground and excited states seperately.

IV. DISCUSSION

A. Mössbauer sites and sample homogeneity

Two Fe sites A and B are observed in the low-temperature Mössbauer spectroscopy on sample SC 1. The main site A is associated with monomer Fe sites without relevant magnetic exchange with other Fe ions since it is observed also in samples SC 2–4 which contain an up to one order of magnitude lower Fe concentration x. Site B is not observed in SC 2–4. We associate site B with a nearest-neighbor in-plane or out-of-plane Fe-dimer site. The magnetic hyperfine field for the two Fe subspecies is determined to $B_A = 70.21(1)$ T and $B_B = 65.0(2)$ T at 2 K. These values are in agreement with Refs. [12,13,15], in which Klatyk *et al.*, Ksenofontov *et al.* have performed a powder study of $x > 0.15$ proposing ferromagnetic ordering for $T < 65$ K.

The temperature dependence of the Mössbauer spectrum shown in Fig. 5 is consistent with the expected behavior of SAM. The observed spin fluctuations are consistently described by a thermal activation crossover rather than by a cooperative long-range ordering transition. However, this does not exclude by itself that Fe site A arises from small cluster-like SMM units like Fe_i clusters in the Li_3N matrix with ferromagnetic interaction between the Fe ions with various size numbers i of Fe depending on x. The deduced hyperfine parameters are within error bars identical for samples SC 1–4. The spin dynamics described by the fluctuation frequency $\nu(T)$, ν_0 and E_A are concentration-independent for Fe site A of SC 1–4. The invariant parameters as a function of x proves well isolated Fe sites like in a SAM.

A combinatorial expression to calculate the probability for n Li ions among six neighbors in the [001] plane for the Fe concentration x yields

$$W_n = 6![n!(6-n)!]^{-1}(1-x)^n x^{6-n} \approx 14\% \tag{26}$$

for $x = 0.027$ and $n = 5$, i.e., an in-plane Fe dimer [12]. This value is twice as large as the observed value. The area contribution of site B is overestimated in this statistical treatment in which every kind of Coulomb repulsion is neglected. Either due to Coulomb repulsion a more homogeneous mononuclear SAM is preferred or an out-of-plane Fe-N-Fe dimer configuration is the observed site B. Interestingly, the total contribution of the Fe-N-Fe in a binomial distribution is supposed to be ≈5.3% which is closer to the experimentally determined value of 5.9(3)% of Fe site B. A systematic Mössbauer study on a

TABLE III. Characteristic Mössbauer parameters obtained at $T \sim 4$ K assuming $\eta = 0$ compared with Zadrozny *et al.* [35].

Compound	δ (mm/s)	ΔE_Q (mm/s)	B (T)
$[Fe(C(SiMe_3)_3)_2]^{1-}$	0.402(1)	−2.555(2)	63.68(2)
$[Fe(C(SiMe_3)_3)_2]$	0.460(3)	−1.275(5)	150.7(1)
$Li_2(Li_{1-x}\ Fe_x)N$ ($x \ll 1$)	0.100(2)	−2.572(2)	70.25(2)

series of $Li_2(Li_{1-x}Fe_x)N$ with larger x on single crystals is needed to identify nearest neighbor Fe-cluster configurations in this system. However, this is beyond the scope of this work.

B. Oxidation and spin state of Fe ions in $Li_2(Li_{1-x}Fe_x)N$

The observed isomer shift value around 0.10 mm/s is unconventional for a Fe oxidation states of Fe^{1+} or Fe^{2+}. It can possibly arise from the linear N-Fe-N low-coordinated electronic structure of Fe in $Li_2(Li_{1-x}Fe_x)N$. Because of the paramagnetic behavior a Fe^{2+} low spin state $S = 0$ can be excluded.

A ^{57}Fe Mössbauer study was performed on the linear complexes [K(crypt-222)][$Fe(C(SiMe_3)_3)_2$] and [$Fe(C(SiMe_3)_3)_2$] with a similar Fe linear coordination by carbon [35]. $[Fe(C(SiMe_3)_3)_2]^{1-}$ in [K(crypt-222)][$Fe(C(SiMe_3)_3)_2$] is proposed to contain Fe^{+1}, whereas Fe^{2+} is present in [$Fe(C(SiMe_3)_3)_2$]. The assumed asymmetry parameter $\eta = 0$ is according to the axial symmetric EFG tensor discussed by Lewis *et al.* [36] (and references therein). Table III shows the values of the isomer shift δ, the quadrupole splitting ΔE_Q and the magnetic hyperfine field B. The smaller δ value of Fe site A can be explained by the increase of s-electron density at the nucleus and the 4s mixing. The EFG value V_{zz}, here given by ΔE_Q of Fe-diluted $Li_2(Li_{1-x}\ Fe_x)N$ (site A) and the Fe^{1+}-SMM, $[Fe(C(SiMe_3)_3)_2]^{1-}$, are very close to each other whereas the Fe^{2+}-SMM shows only half of this value. Moreover, also the magnetic hyperfine fields of $[Fe(C(SiMe_3)_3)_2]^{1-}$ and Fe-diluted $Li_2(Li_{1-x}\ Fe_x)N$ are comparable. Therefore, we conclude a strong similarity of the Fe electronic systems in these two systems with oxidation state Fe^{+1} for $Li_2(Li_{1-x}Fe_x)N$. An oxidation state of Fe^{1+} is also consistent with calculated electronic band structure [12,30].

C. Energy barrier and spin dynamics

Figure 15 shows the temperature dependence of the spin fluctuation rate of SC 1, determined from Mössbauer spectroscopy, ac susceptibility and direct magnetization relaxation measurements, respectively. At three Mössbauer data points at $1/T \gg 0.05$ K^{-1}, essentially static Mössbauer spectra are measured, i.e., the fluctuation rate becomes smaller than the lower bound of the frequency window of the method and these data points are not shown. The quantum tunneling regime with a nearly constant low fluctuation frequency of the order of 0.01 s^{-1} is reached for temperatures below ≈15 K, i.e., $1/T > 0.08$ K^{-1} in Fig. 15.

The relaxation rates, ν, obtained by Mössbauer and ac susceptibility measurements can be well described by a

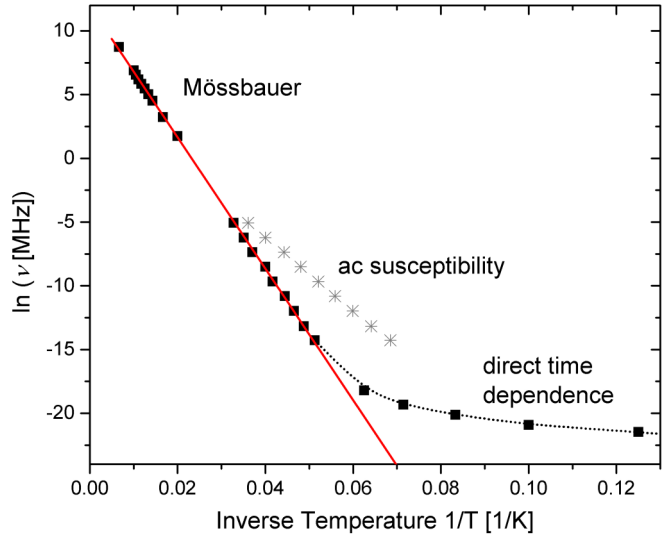

FIG. 15. Fluctuation frequencies of SC 1 determined by Mössbauer spectroscopy, ac susceptibility and magnetization relaxation measurements (direct time dependence), shown in form of an Arrhenius plot. The red line shows a fit to the high temperature region and yields an effective energy barrier of $\bar{E}_A = 515(20)$ K. The gray points describe a second low frequency activated relaxation process with an activation energy of $\bar{E}_A = 270(12)$ K, observed in the ac susceptibility at low temperatures.

single effective energy barrier of $\bar{E}_A = 515(20)$ K. Note that there is another, larger peak observable in the temperature-dependent ac susceptibility that corresponds to a faster relaxation with an effective energy barrier of $\bar{E}_A = 270(12)$ K (grey stars in Fig. 15). The pre-exponential factor of the Arrhenius behavior amounts to $\nu_0 = 150(10)$ GHz. We conclude that this relaxation process is enhanced by the application of transverse magnetic fields and becomes visible in the Mössbauer frequency window (see Sec. III D above). The deduced activation energies are consistent within error bars. For $T < 10$ K the relaxation rates were determined by fitting the time-dependent magnetization to stretched exponential $M(t) = M_0 \exp[-(t\nu)^\beta]$.

At zero external field, the two allowed phonon-assisted relaxation processes $J_z = -7/2 \rightarrow J_z = 5/2$ and $J_z = 7/2 \rightarrow J_z = -5/2$ have equal energy differences. They become non-equal under applied longitudinal magnetic field as presented above. The direct quantum tunneling regime is reached below 10 K (see Fig. 15).

In Table IV, we compare the thermal activation energy barriers for several SAM systems with large energy barriers

TABLE IV. Selected SAMs with a large energy barrier E_A and the corresponding paramagnetic ion.

Compound	magn. unit	E_A (K)	Reference
[Dy(bbpen)X]	Dy^{3+}	1025	[37]
TbBis(phthalocyaninate)	Tb^{3+}	940	[38]
$Li_2(Li_{1-x}\ Fe_x)N$	Fe^{1+}	570(6)	this work
$[Fe(C(SiMe_3)_3)_2]^{1-}$	Fe^{1+}	354	[35,39]
$[Sr_{10}(PO_4)_6(Cu_x\ OH_{1-x-y})_2]$	Cu^{3+}	69	[40]

E_A compared to Fe-diluted $Li_2(Li_{1-x}\ Fe_x)N$. The thermal activation barrier E_A is often associated with a two-phonon Orbach process [22]. Above 50 K, the dominant character of this process is plausible: the direct spin transition process in the Debye model accompanied by the creation or annihilation of a single phonon is dominant only for lower temperature $T < 50$ K with $\tau_S^{-1} \propto T$.

In the literature, the energy barrier is often identified with the zero-field splitting value D rather than considered as an effective experimental quantity, which depends on different microscopic parameters as discussed above. However, as demonstrated by our spin Hamiltonian approach, the energy barrier is a function of the (internal or applied) transverse magnetic field and a general scaling proportional to $(2J+1)^{4/3}$ [cf. Eq. (23)]. The effective spin Hamiltonian calculation presented in this work can qualitatively account for the temperature and transverse field dependencies of the experimentally observed spin fluctuation rates.

The spin dynamics in applied longitudinal magnetic fields can be understood considering the Zeeman shift of the J_z states which induces a splitting of the spin fluctuation rate into two branches. The observed experimental asymmetry is expected theoretically and is caused by higher-order Stevens' operator terms produced by the hexagonal symmetry of the lattice.

V. CONCLUSIONS

In this work, we present ^{57}Fe Mössbauer studies on diluted Fe centers in a linear N-Fe-N configuration along the crystallographic c axis in single crystalline specimen of hexagonal $Li_2(Li_{1-x}Fe_x)N$. The homogeneity of the nanoscale distributed isolated Fe centers is shown and the single-atomic magnet nature confirmed. Below 30 K, the magnetically isolated single-ion Fe centers exhibit a large quasistatic magnetic hyperfine field of $\bar{B}_A = 70.25(2)$ T parallel to the c axis, which is the strongest principle axis of the electric field gradient $\bar{V}_{zz} = -154.0(1)$ V/Å^2.

Fluctuations of the magnetic hyperfine field clearly observed in the Mössbauer spectra between 50 and 300 K are described by a Blume two-level relaxation model. The spin dynamics in $Li_2(Li_{1-x}Fe_x)N$ is concentration-independent for $x \leqslant 0.028$. From the temperature dependence an Orbach process is deduced as the dominant spin-lattice relaxation process. An Arrhenius analysis $\nu = \nu_0 e^{-E_A/k_BT}$ yields a thermal activation barrier of $\bar{E}_A = 515(20)$ K and an attempt frequency $\bar{\nu}_0 = 150(10)$ GHz. Mössbauer spectroscopy studies with applied transverse magnetic fields up to 5 T reveal a huge increase of the fluctuation rate by two orders of magnitude. In applied longitudinal magnetic fields a characteristic splitting of the spin fluctuation frequency is observed. These experimental observations are qualitatively reproduced by a single-ion spin Hamiltonian analysis. It demonstrates that for dominant magnetic quantum tunneling a weak axial single-ion anisotropy D of the order of a few Kelvin can cause a two orders of magnitude larger energy barrier for temperature-induced longitudinal spin fluctuations. We think that this is one of the most spectacular manifestations of the macroscopic quantum spin tunneling observed in the solid-state based single-atomic magnet $Li_2(Li_{1-x}\ Fe_x)N$. The experiments suggest $Li_2(Li_{1-x}Fe_x)N$ to be a candidate for novel functional magnetic materials, e.g., for quantum computing or spintronic devices.

TABLE V. Mass absorption coefficients μ_a according to Chen *et al.* and therein [21].

Element	Atomic mass (u)	absorption coefficient (cm^2/g)
Li	3	0.277
N	7	1.4
Fe	26	64
Os	76	165

ACKNOWLEDGMENTS

This work was supported by the Deutsche Forschungsgemeinschaft (DFG, German Research Foundation) through SFB 1143 and JE748/1. Special thanks to J. Schnack, M. Baker, and E. Bill for helpful and constructive remarks.

APPENDIX A: MASS ABSORPTION COEFFICIENTS

The Fe concentration of sample SC 4 is with below 0.2% rather small, even for a ^{57}Fe Mössbauer experiment of a non-^{57}Fe-enriched sample. $Li_2(Li_{1-x}Fe_x)N$ contains only light elements with small absorption coefficients of the 14.41 keV radiation energy, see table V. The mass absorption coefficient μ_a describes the exponential Intensity reduction of the initial γ-ray intensity I_0,

$$I(d) = I_0(1 - f_s)e^{\mu_a d}, \tag{A1}$$

where d is the absorber thickness and f_s the recoil-free fraction of transitions. μ_a describes the non-resonance atomic absorption, mainly by the photoelectric effect. For a comparison, the value of Osmium represents a heavy element in table V showing the rather small mass absorption coefficient μ_a of Li and N since Fe is highly diluted. We have used for this reason large crystals of a thickness of a few millimeter and the effective thickness $t_a = 2.39(10)$ of SC 1 reflects still absorption far away from the saturation limit. The Fe concentration of SC 4 is even below the concentration of Ho in $LiY_{0.998}\ Ho_{0.002}\ F_4$ or at least in the same order which is a prominent example for a SAM in a solid crystal [41,42].

APPENDIX B: MAGNETIC HYPERFINE FIELD

The results of the calculations are discussed assuming the Fe^+ oxidation state [30]. In general, the total magnetic hyperfine field B is the sum of different contributions

$$B_h = B_c + B_{\rm orb} + B_{\rm dip} + B_{\rm lat}. \tag{B1}$$

The sign of the Fermi contact contribution B_c is negative and arises from the spin polarization of the s electrons by unpaired valence electrons. $B_{\rm orb}$ is the orbital contribution scaling with the orbital quantum number L which is expected to be nonzero since the observed value of important because of the exceeded spin only value of the magnetic moment. $B_{\rm dip}$ is the dipolar contribution arising from nonsperical electron spin density contribution which is approximately proportional to V_{zz}. $B_{\rm lat}$ is the lattice contribution, i.e., the magnetic field generated by

neighbor electronic moments in the lattice. This contribution can be neglected in the diluted system. The detailed values depend on the used computational method [30]. The general result is that $B_{\rm orb}$ is the dominant contribution and ≈10 times stronger and of opposite sign as B_c for the Fe^{1+} ($S = 3/2$, $L = 2$) state [30].

APPENDIX C: MAGNETIZATION HYSTERESIS LOOPS

The presented hysteresis loops of magnetization were measured at different temperatures for magnetic fields applied parallel to the crystallographic c axis, $B \parallel c$. The obtained data were corrected for the diamagnetic sample holder (sample sandwiched between two torlon discs and fixed inside a straw) for which the magnetization was determined separately using a similar setup. The diamagnetic contribution of the α-Li_3N host was subsequently subtracted from the sample holder corrected data using $\rho(Li^{1+}) = -8.8 \times 10^{-12}$ m^3 mol^{-1} [43] and $\rho(N^{3-}) = 1.63 \times 10^{-10}$ m^3 mol^{-1} [44].

APPENDIX D: BREIT-WIGNER FORMULA

The cross-section

$$\sigma(E) = \frac{\sigma_a(E)}{\sigma_0} \tag{D1}$$

of the transmission integral is given by the Breit-Wigner formula

$$\sigma_0(E) = \frac{\sigma_0 \Gamma_a^2/4}{(E - E_0)^2 + \Gamma_a^2/4}, \tag{D2}$$

where

$$\sigma_0 = \left(\frac{\lambda^2}{2\pi}\right)\frac{1 + 2I_{(e)}}{1 + 2I_{(g)}}\frac{1}{1 + \alpha} \tag{D3}$$

is the maximum cross section, e.g., see Chen [21]. Here, α is the internal conversion coefficient, $I_{(e)}$,$I_{(g)}$ are the nuclear spin numbers of the ground state and excited state, respectively, and λ the energy of the γ ray. $\sigma(E)$ and $\sigma_0(E)$ are given as a function of the photon energy E, E_0 is the energy of the γ ray corresponding to the Mössbauer transition. The excited state is not strict monochromatic and has a natural distribution given by a Lorentzian line

$$L(E)dE = \frac{\Gamma_s}{2\pi}\frac{1}{(E - E_0)^2 + \Gamma_s^2/4}dE \tag{D4}$$

with

$$\int L(E)dE = 1. \tag{D5}$$

Γ_s is the natural linewidth of the Mössbauer nuclei and Γ_a is the natural linewidth of the absorber. Here,

$$L(E, v) = L\left(E - \frac{v}{c}E_0\right) \tag{D6}$$

is the relation to our notation with the speed of light c.

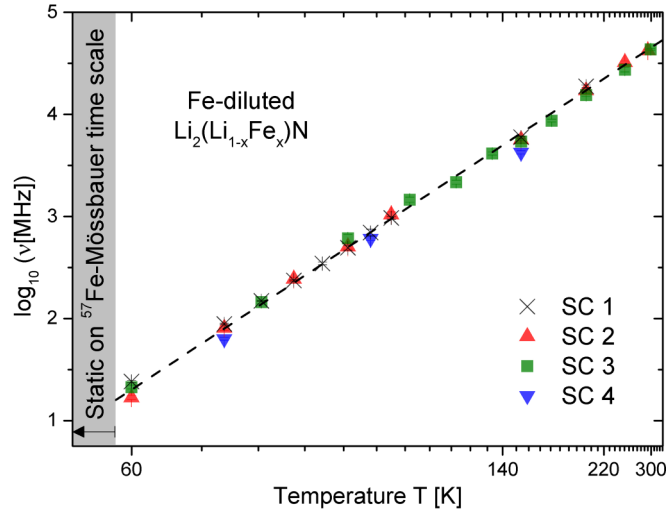

FIG. 16. Logarithmic frequency $\log_{10}\nu$ of Fe site A of SC 1–4 as a function of temperature.

APPENDIX E: ARRHENIUS PLOT

Figure 16 shows the Arrhenius plot (reciprocal T scaling)

$$\ln \nu = \ln \nu_0 - \frac{E_A}{k_B}\left(\frac{1}{T}\right) \tag{E1}$$

of the extracted fluctuation frequencies $\ln\nu$ of SC 1–4 in MHz. The fluctuation frequency is concentration independent as reflected by the parameter E_B and $\ln\nu_0$ of table II.

APPENDIX F: LANDÉ FACTOR

To estimate the Zeeman splitting, it is important to recall the large effective magnetic moment $\mu_{\rm eff} = 6.5(4)\mu_B$ per Fe atom parallel to the c axis [14] which is close to the full Hunds' rule value of Fe^+. This indicates the validity of the Hunds' rules in this system. Using Russel-Saunders coupling and the proposed spin quantum number $L = 2$ and $S = 3/2$,

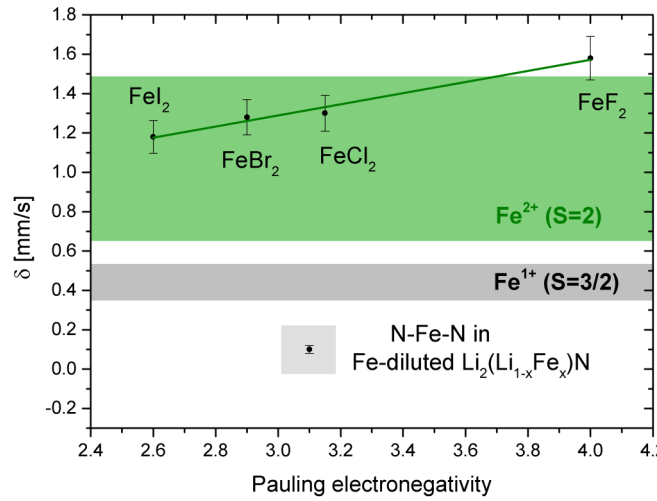

FIG. 17. Isomer shift relative to α-iron as a function of the Pauling electronegativity of the ferrous halides compared with SC 1 [45].

TABLE VI. Comparison of the Debye-temperature Θ_D for $Li_2(Li_{1-x}Fe_x)N$ with results for similar linear Fe^{1+} and Fe^{2+} complexes [35].

Compound	Θ_D (K)
$[Fe(C(SiMe_3)_3)_2]^{1-}$	313(16)
$[Fe(C(SiMe_3)_3)_2]$	125(1)
$Li_2(Li_{1-x}\ Fe_x)N$	315(8)

we get the Landé factor for $J = 7/2$,

$$g_J = \frac{3}{2} + \frac{S(S+1) - L(L+1)}{2J(J+1)} \approx 1.43. \qquad \text{(F1)}$$

Here, $g_L = 1$ and $g_S = 2$ are used.

APPENDIX G: COMPARISON WITH FERROUS HALIDES

Axtmann *et al.* have found a linear relationship between the Pauling electronegativity and the isomer shift δ in ferrous halides is discussed [45]. The difference of the ligand electronegativity is related to the isomer shift. This is treated as direct evidence for the participation of 4*s* electrons in the formation of the chemical bonds [21]. Figure 17 shows the presented ferrous halides by Axtmann *et al.* and the isomer shift of SC 1. The observed isomer shift deviates strongly. In the ferrous halides, the electronic configuration is $3d4s^x$ where x measures the ionicity. The ionicity increased with x [21]. The electric monopole hyperfine interaction in $Li_2(Li_{1-x}Fe_x)N$ is far away from the values of the Fe^{2+} ferrous halides. The quadrupole splitting in the ferrous halides behaves linear as a function of the isomer shift as well [45]. The values are between 1.4 mm/s (FeI_2) and 2.6 mm/s (FeF_2). For conversion [20], one can use

$$\Delta v_{QS} = \frac{ceQ}{2E_\gamma} V_{zz} \sqrt{1 + \frac{\eta^2}{3}} \qquad \text{(G1)}$$

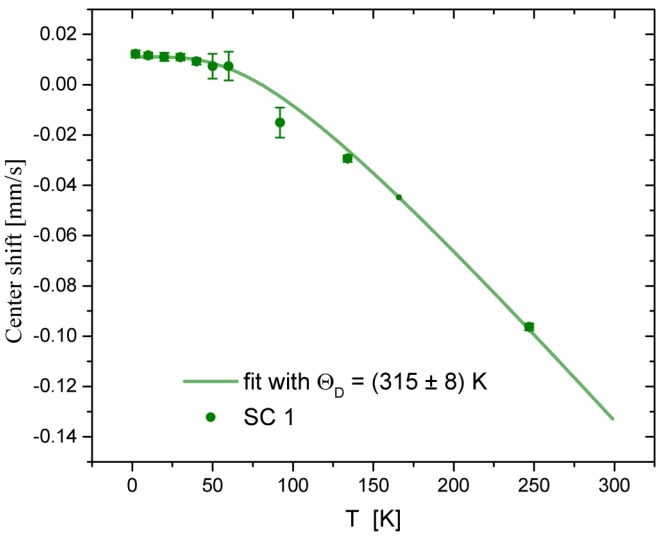

FIG. 18. Center shift as a function of the temperature and fit to determine the Debye temperature Θ_D.

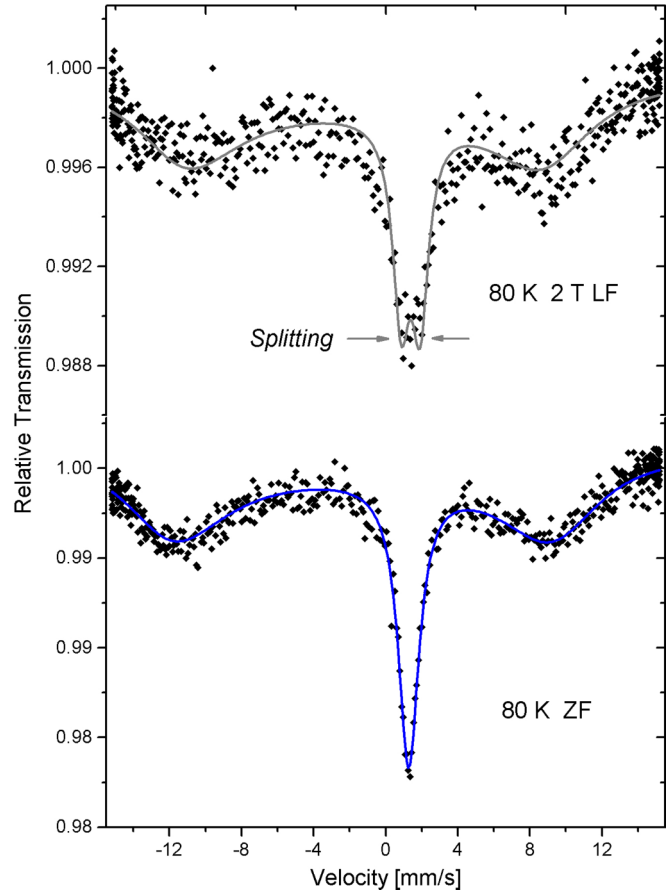

FIG. 19. Comparison of the Mössbauer measurements at 80 K in ZF and in an applied longitudinal field of 2 T. The fit model is described in the main text.

with

$$\frac{ceQ}{2E_\gamma} \approx 0.0167 \frac{\text{mm/s}}{\text{V/Å}^2}. \qquad \text{(G2)}$$

The value of Fe-diluted $Li_2(Li_{1-x}Fe_x)N$ is $-2.572(2)$ mm/s, which shows a comparable electric quadrupole hyperfine interaction with respect to the amount of V_{zz}.

APPENDIX H: DETERMINATION OF THE DEBYE-TEMPERATURE Θ_D

Figure 18 shows the center shift as a function of temperature obtained in ZF of SC 1. The center shift is here $\delta + \delta_{SOD}$ without α-iron correction and therefore relative to the ^{57}Co source. The temperature dependence of SC 1 yielded a Debye temperature of $\Theta_D = 315(8)$ K which is a measure of the collective motion of the surrounding atoms of the Mössbauer nucleus. One should keep in mind the special geometry with the γ beam parallel to the crystallographic c axis and therefore the phonic excitations in c-direction are considered according to the Debye-Waller factor. In Table VI, we compare this value with the aforementioned linear C-Fe-C compounds. The values for $[Fe(C(SiMe_3)_3)_2]^{1-}$ and $Li_2(Li_{1-x}Fe_x)N$ are similar. This fact further supports the conclusion of a similar electronic configuration of the Fe ion drawn from the values of the quadrupole splitting ΔE_Q and the magnetic

hyperfine field B_A in $Li_2(Li_{1-x}Fe_x)N$ compared to those of $[Fe(C(SiMe_3)_3)_2]^{1-}$.

APPENDIX I: ^{57}Fe-MÖSSBAUER MEASUREMENT AT 80 K IN 2 T LF of $Li_2(Li_{1-x}Fe_x)N$

Figure 19 shows a comparison of the ^{57}Fe Mössbauer measurements at 80 K in ZF and in an applied longitudinal field of 2 T of SC 1. The analysis is done in the same way as discussed in the main text. The intermediate relaxation line splits at 80 K in a magnetic field of 2 T LF. The doublet is weakly adumbrated because of the scattering of the data (lower magnitude of absorption) and not so well pronounced like in the presented 100 K measurement at 2 T. However, a splitting is confirmed. The grey fit is the result of free convergence of the mentioned two-frequency spin reversal model. The relaxation frequencies are $\log_{10}\nu_{\mathrm{up}} = 2.63(8)\log_{10}[\mathrm{MHz}]$ and $\log_{10}\nu_{\mathrm{down}} = 2.36(6)\log_{10}[\mathrm{MHz}]$, therefore $\nu_{\mathrm{up}} \approx 427$ MHz and $\nu_{\mathrm{down}} \approx 229$ MHz.

[1] D. Gatteschi and R. Sessoli, Angew. Chem., Int. Ed. **42**, 268 (2003).
[2] D. Gatteschi, R. Sessoli, and J. Villain, *Molecular Nanomagnets* (Oxford University Press, Oxford, 2006).
[3] L. Bogani and W. Wernsdorfer, Nat. Mater. **7**, 179 (2008).
[4] T. O. Strandberg, C. M. Canali, and A. H. MacDonald, Nat. Mater. **6**, 648 (2007).
[5] M. N. Leuenberger and D. Loss, Nature (London) **410**, 789 (2001).
[6] C. Zener, Proc. R. Soc. A **137**, 696 (1932).
[7] L. Thomas, F. Lionti, R. Ballou, D. Gatteschi, R. Sessoli, and B. Barbara, Nature (London) **383**, 145 (1996).
[8] C. Sangregorio, T. Ohm, C. Paulsen, R. Sessoli, and D. Gatteschi, Phys. Rev. Lett. **78**, 4645 (1997).
[9] D. Loss, D. P. DiVincenzo, and G. Grinstein, Phys. Rev. Lett. **69**, 3232 (1992).
[10] W. Wernsdorfer and R. Sessoli, Science **284**, 133 (1999).
[11] J. Klatyk and R. Kniep, Z. Kristallogr. - New Cryst. Struct. **214**, 447 (1999).
[12] J. Klatyk, W. Schnelle, F. R. Wagner, R. Niewa, P. Novák, R. Kniep, M. Waldeck, V. Ksenofontov, and P. Gütlich, Phys. Rev. Lett. **88**, 207202 (2002).
[13] V. Ksenofontov, S. Reiman, M. Waldeck, R. Niewa, R. Kniep, and P. Gütlich, Zeitschrift für anorganische und allgemeine Chemie **629**, 1787 (2003).
[14] A. Jesche, R. W. McCallum, S. Thimmaiah, J. L. Jacobs, V. Taufour, A. Kreyssig, R. S. Houk, S. L. Bud'ko, and P. C. Canfield, Nat. Commun. **5**, 3333 (2014).
[15] M. Fix, A. Jesche, S. G. Jantz, S. A. Bräuninger, H.-H. Klauss, R. S. Manna, I. M. Pietsch, H. A. Höppe, and P. C. Canfield, Phys. Rev. B **97**, 064419 (2018).
[16] M. Fix, J. H. Atkinson, P. C. Canfield, E. del Barco, and A. Jesche, Phys. Rev. Lett. **120**, 147202 (2018).
[17] L. Xu, Z. Zangeneh, R. Yadav, S. Avdoshenko, J. van den Brink, A. Jesche, and L. Hozoi, Nanoscale **9**, 10596 (2017).
[18] A. Jesche and P. C. Canfield, Philos. Mag. **94**, 2372 (2014).
[19] P. C. Canfield and I. R. Fisher, J. Cryst. Growth **225**, 155 (2001).
[20] S. Kamusella and H.-H. Klauss, Hyperfine Interact. **237**, 82 (2016).
[21] Y. Chen and D.-P. Yang, *Mössbauer Effect in Lattice Dynamics: Experimental Techniques and Applications* (Wiley-VCH, John Wiley, 2007).
[22] P. Guetlich, E. Bill, and A. X. Trautwein, *Moessbauer Spectroscopy and Transition Metal Chemistry* (Springer, Berlin, Heidelberg, 2011), DOI:10.1007/978-3-540-88428-6.
[23] M. A. Chuev, J. Phys.: Condens. Matter **23**, 426003 (2011).
[24] K. Faid and R. F. Fox, Phys. Rev. A **34**, 4286 (1986).
[25] M. Blume, Phys. Rev. **174**, 351 (1968).
[26] P. Carretta and A. Lascialfari (eds.), *NMR, μSR and Mössbauer Spectroscopy in Molecular Magnets* (Springer, Berlin, Heidelberg, 2007).
[27] E. Segal and W. Wallace, J. Solid State Chem. **2**, 347 (1970).
[28] E. Segal and W. Wallace, J. Solid State Chem. **6**, 99 (1973).
[29] E. Segal and W. Wallace, J. Solid State Chem. **11**, 203 (1974).
[30] P. Novák and F. R. Wagner, Phys. Rev. B **66**, 184434 (2002).
[31] V. Ulyanov and O. Zaslavskii, Phys. Rep. **216**, 179 (1992).
[32] O. B. Zaslavskii, Phys. Rev. B **42**, 992 (1990).
[33] M. Enz and R. Schilling, J. Phys. C: Solid State Phys. **19**, L711 (1986).
[34] R. Orbach and B. Bleaney, Proc. R. Soc. A **264**, 485 (1961).
[35] J. M. Zadrozny, D. J. Xiao, J. R. Long, M. Atanasov, F. Neese, F. Grandjean, and G. J. Long, Inorg. Chem. **52**, 13123 (2013).
[36] J. Lewis and D. Schwarzenbach, Acta Crystallogr., Sect. A **37**, 507 (1981).
[37] J. Liu, Y.-C. Chen, J.-L. Liu, V. Vieru, L. Ungur, J.-H. Jia, L. F. Chibotaru, Y. Lan, W. Wernsdorfer, S. Gao, X.-M. Chen, and M.-L. Tong, J. Am. Chem. Soc. **138**, 5441 (2016).
[38] C. R. Ganivet, B. Ballesteros, G. de la Torre, J. M. Clemente-Juan, E. Coronado, and T. Torres, Chem. - Eur. J. **19**, 1457 (2013).
[39] J. M. Zadrozny, D. J. Xiao, M. Atanasov, G. J. Long, F. Grandjean, F. Neese, and J. R. Long, Nat. Chem. **5**, 577 (2013).
[40] P. E. Kazin, M. A. Zykin, Y. V. Zubavichus, O. V. Magdysyuk, R. E. Dinnebier, and M. Jansen, Chem. - Eur. J. **20**, 165 (2014).
[41] R. Giraud, A. M. Tkachuk, and B. Barbara, Phys. Rev. Lett. **91**, 257204 (2003).
[42] R. Giraud, W. Wernsdorfer, A. M. Tkachuk, D. Mailly, and B. Barbara, Phys. Rev. Lett. **87**, 057203 (2001).
[43] J. Banhart, H. Ebert, J. Voitländer, and H. Winter, J. Magn. Magn. Mater. **61**, 221 (1986).
[44] P. Höhn, S. Hoffmann, J. Hunger, S. Leoni, F. Nitsche, W. Schnelle, and R. Kniep, Chem. Eur. J. **15**, 3419 (2009).
[45] R. C. Axtmann, Y. Hazony, and J. W. Hurley, Jr., Chem. Phys. Lett. **2**, 673 (1968).